Applied Energy 399 (2025) 126457

Contents lists available at ScienceDirect

Applied Energy

journal homepage: www.elsevier.com/locate/apenergy

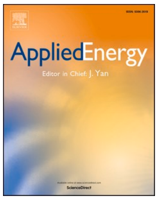

Parallax and cloud shadow correction in satellite-based solar irradiance estimation: A study in tropical environments

Arindam Roy [a,*], Annette Hammer [a], Detlev Heinemann [b], Marion Schroedter-Homscheidt [a], Ontje Lünsdorf [a], Jorge Lezaca [a]

[a] *German Aerospace Center (DLR), Institute of Networked Energy Systems, Oldenburg, Germany*
[b] *University of Oldenburg, Institute of Physics, Oldenburg, Germany*

HIGHLIGHTS

- Applied parallax and cloud shadow shifts, estimated from gridded CTH, to cloud index images via bilinear interpolation.
- Mean rel. RMSE in GHI fell from 23.8 % to 22.1 %, with larger drops at higher satellite viewing zenith angles θ_{sza}.
- Corrected Heliosat-3 GHI shows 4–7 percentage points lower rel. RMSE than NSRDB and CAMS, for sites with similar θ_{sza} values.
- The corrections have no effect when the CTH is below 2 km.
- Swinging Door ramp score shows improvement within a range of GHI ramp threshold values relevant for cloud-induced changes.

ARTICLE INFO

Keywords:
Earth observation
Global horizontal irradiance (GHI)
Satellite viewing parallax
Heliosat-3 method
Cloud top height (CTH)
Cloud shadow projection
Meteosat-8
NSRDB
CAMS Himawari

ABSTRACT

Accurate estimation of Global horizontal solar irradiance (GHI) from geostationary satellite imagery is essential for intraday solar PV power forecasting. Tropical regions show an even more challenging situation: A typically much higher tropopause results in higher cloud tops and correspondingly larger parallax errors in satellite imagery with significantly larger cloud shadow displacements compared to mid-latitudes. This study improves GHI estimates from Meteosat-8 by correcting cloud parallax and shadow displacement using gridded cloud top height (CTH) data. Fractional or sub-pixel displacement of individual cloudy pixels is enabled by bilinear interpolation in contrast to prior methods that allowed only integer shifts or assigned a single CTH value to a grouping of adjacent cloud pixels. Validation against one year of 15-min resolution ground-based measurements at five sites in South and Southeast Asia shows a reduction in relative root mean square error (rel. RMSE) from 23.8 % to 22.1 %. Improvements are more pronounced at higher satellite viewing zenith angles (θ_{sza}) and in the presence of high-altitude clouds. The corrected satellite-based GHI exhibits 4–7 percentage points lower rel. RMSE than National Solar Radiation Database (NSRDB) and 2.5 points lower than CAMS solar radiation service for similar θ_{sza}. Greatest error reductions occur during partly cloudy conditions for sites within 61° θ_{sza}, and under overcast skies for sites close to the edge of Meteosat-8's field of view. Improvements also depend on the co-scattering angle between sun and satellite with respect to the site, and the availability of sufficient upstream cloud information along the path of solar irradiance falling on the site. Ramp detection accuracy improves, particularly at lower detection thresholds, as measured using the Swinging Door Algorithm.

1. Introduction

Motivated by the drastic effects of climate change, the United Nations (UN) has introduced the 2030 Sustainable Development Goals (SDGs). Ensuring affordable and clean energy is an integral part of these goals [1]. Solar PV is expected to account for half of all renewable power expansion worldwide from 2021 to 2026 [2], with a significant portion being installed in tropical regions due to abundant solar radiation. However, power output from solar PV is variable, primarily due to cloud shadows causing fluctuations in power generation [3–5]. This variability affects the economic operation of generators, the energy market's reliability, and the secure operation of the electricity grid [6].

---

[*] Corresponding author.
E-mail address: arindam.roy@dlr.de (A. Roy).

https://doi.org/10.1016/j.apenergy.2025.126457
Received 14 October 2024; Received in revised form 14 June 2025; Accepted 9 July 2025

Long-term estimates of global horizontal irradiance (GHI) from geostationary satellites are often used in deciding PV site locations in the absence of ground-measured data [7,8]. In Ohtake et al. [9], the authors estimated the PV power generation of a region from satellite images and validated them against measurements from the Transmission System Operator (TSO). Jamaly et al. [10] assessed the ability of satellite estimated irradiance to track large ramps in the aggregate power output of PV systems distributed across an entire transmission grid area. Clouds are one of the most important sources of uncertainty in satellite-retrieved GHI [11,12]. From a system operator point of view, data on ramp behavior of the aggregate solar PV output induced by clouds, is particularly important for real-time monitoring and the control strategies for maintaining load-generation balance in the electricity grid [13,14]. However, satellite based global horizontal irradiance (GHI) estimation and forecasting methods have been primarily developed for the mid-latitudes. Large errors in satellite-based forecasts of GHI are observed during the monsoon season in tropical regions due to the increased formation and dissipation of clouds as a result of the intense atmospheric convection [15].

The tropical tropopause layer (TTL) is a transition zone from the turbulent troposphere to the radiatively controlled stratosphere and acts as a physical boundary for the vertical expansion of clouds [16]. The TTL extends from 14 km to altitudes exceeding 18 km during periods of deep convection [17]. The height of the tropopause steeply drops in the mid-latitudes and reaches 8–12.5 km in the high latitudes [18]. Consequently, clouds at higher altitudes are observed more frequently over the tropics that cause a larger parallax shift in cloud locations on satellite images and a larger displacement of cloud shadows from the actual cloud than observed in the mid-latitudes. In a worldwide benchmark of solar irradiance models, consistently lower accuracy in satellite estimated GHI was observed in the tropical regions compared to the mid-latitudes [19]. Deep convective clouds (DCC) with cumulus towers, overshooting tops and accompanying outflowing cirrus clouds are common during the seasonal monsoons in the tropical and subtropical regions [20,21]. Although the Southwest summer monsoon affects larger parts of South and Southeast Asia, the Northeast winter monsoon also strongly impacts some parts in this region [22]. Pre-summer monsoon thunderstorms or Nor'westers are frequently observed during April–May in the eastern and northeastern parts of the Indian subcontinent [23,24].

Several authors reported the parallax of the satellite viewing angle as a source of error in satellite-retrieved GHI [25–34]. The error in estimated GHI at a site increases with the distance of the site from the sub-satellite point (SSP) at the equator due to the increasing satellite viewing angle [32], and with the increase in cloud top height (CTH) [35]. The parallax in cloud location caused by the satellite viewing angle and the displacement of the shadow from the actual cloud location results in faulty estimation of ramps from satellite images. Due to the large area covered by a satellite pixel, accurate information on cloud position and height is not easy to obtain. Accurate cloud base height (CBH) measurements can be obtained from ceilometer measurements, but only for single points [36]. CBH and cloud top height (CTH) can be triangulated using multiple sky-imagers, and to a certain extent multi-camera stereography can detect multi-layer clouds with voxel carving [37]. However, the spatial extent over which such information is available is limited by the location and size of the camera network and therefore cannot be derived for all locations on a satellite image of the Earth disk. Satellite infrared (IR) channel images can be used to derive cloud top temperature and height [38]. However, such estimations are also prone to error in situations with multi-layered clouds and very low or very large cloud heights [39]. The IR channel derived CTH does not produce suitable estimates for semitransparent clouds [40] or broken clouds smaller than the IR pixel resolution [41], due to the contribution from the part of the ground below. This introduces further inaccuracies into the parallax and cloud shadow displacement calculations. High elevation and complex terrain geometry can further introduce errors, as observed in the case of high convective clouds in Dürr et al. [42]. Marie-Joseph et al. [43] reported the highest errors due to the satellite viewing parallax in partly cloudy conditions. In the case of clouds with low CTH, as observed by Wu et al. [44] for coastal stratocumulus clouds with an average CTH of 400 m above the mean sea level (MSL), the parallax effect is small relative to the scale of terrain elevation changes and the horizontal resolution of the satellite images. Sossan [45] performed load flow calculations for different levels of distributed PV systems in a medium and low voltage electrical network to characterize the variability of power flow at the Grid Connection Point (GCP). They observed the largest underestimation of variability from satellite data during nearly clear-sky days due to small clouds, reduced spatiotemporal resolution, and parallax effects. Kallio-Myers et al. [46] observed that the parallax error is more significant at higher latitudes, but the correction is harder to apply due to the larger satellite viewing angles. Tatsiankou et al. [47] estimated the lower bound of the parallax error to be somewhere between 5 % and 12 % relative root mean square error (rel. RMSE), with GHI data at 30 min temporal resolution. However, they did not perform any kind of correction to the dataset.

Some studies have already introduced methods to account for the parallax in the satellite viewing angle. Deneke et al. [48] attempted to mitigate parallax error by spatially averaging 3 × 3 pixels around any site, although the parallax effect is not spatially uniform across the entire image. Deneke et al. [49] estimated the shift by finding the pixel in a neighborhood around the site with the highest correlation in satellite-estimated GHI. Lorenzo et al. [50] corrected the geolocation of cloud shadows in the University of Arizona Solar Irradiance Based on Satellite (UASIBS) and the State University of New York GOES satellite-based solar model (SUNY). The optimal match between satellite estimated and ground-measured GHI was found by iterating over a range of CTH values from 0 to 14 km, assumed to be uniform over the 75 km × 80 km image section analyzed. However, the CTH distribution is not uniform in reality, especially for the large image sections needed to predict approaching cloud shadows hours in advance. Furthermore, these correlation-based approaches require real-time ground truth data, limiting their operational and spatial applicability. Deneke et al. [51] estimated the parallax shift in SEVIRI cloud images using MODIS images of the same area by maximizing the cross-correlation between the two. This method is inherently limited by the availability of Low Earth Orbit (LEO) satellite images, which only make limited overpasses in a day over a given location. In operational settings, correcting parallax in geostationary imagery requires a gridded CTH dataset updated at the same temporal resolution as the imagery.

Li et al. [52] proposed a method based on infrared brightness temperature to identify and match cloud shadows, but the inability of IR channels to distinguish cloud shadows from water bodies limits its robustness. Moreover, the method's effect on GHI estimation was not assessed. Bieliński [53] augmented Vicente et al. [54]'s parallax correction to improve rain cloud localization using gridded CTH, validated against radar data, but did not extend this to cloud shadows or GHI accuracy.

Beyer et al. [55] calculated the satellite viewing parallax and cloud shadow displacements using a gridded CTH data, and applied it on the cloud index (CI) images in the Heliosat procedure. The accuracy of the method was validated by observing the improvement in the linear fit between ground-measured clear sky index k_c and CI with two months of data over a limited area spanning 48° N to 54.2° N and 6.7° E to 13.3° E. However, the CI values were shifted in discrete steps by reassigning to the nearest pixel, which can introduce abrupt transitions and loss of subpixel detail. Furthermore, the reduction in error of the estimated GHI was not evaluated on a dataset large enough to account for the variations in cloud type, cloud height and sun-site-satellite geometry due to the seasonal influence. In Miller et al. [56], the authors grouped adjacent cloudy pixels into individual cloud objects with a mean height and averaged cloud properties before applying the geometric correction described in Vicente et al. [54]. While this grouping strategy reduced computational complexity by applying the same parallax and shadow displacement to all the cloudy pixels within a group, it does not allow for the independent displacement of individual adjacent cloudy pixels with different cloud heights. As a result, introduces smoothing effects that could obscure variations in cloud shadow geometry for heterogeneous cloud fields. Furthermore, the validation of the reduction in error due to the correction was not shown. Bright [57] uses a pixel-shifting approach for correcting the parallax in satellite-estimated solar irradiance datasets. However, a detailed description of the method and an analysis of the improvement in GHI estimation is missing.

In contrast to these studies, a pixel-level parallax and cloud shadow correction approach for Heliosat-3 CI images using gridded CTH data and bilinear interpolation is proposed in this work. This addresses three key limitations in prior work: (1) coarse spatial correction due to nearest pixel rounding or group averaging, (2) dependence on sparse or delayed ground truth or LEO imagery; and (3) lack of validation across diverse weather conditions, particularly in the tropics.

Following Beyer et al. [55], we neglect Earth curvature when computing the parallax and cloud shadow shifted latitude-longitude coordinates of each cloudy CI pixel, but perform the CI remapping step with bilinear interpolation to allow for non-integer pixel displacements. This avoids hard reassignment to the nearest pixel, as in Beyer et al. [55], or smoothing due to group-averaged properties, as in Miller et al. [56], preserving local spatial structure and making the method suitable for complex cloud scenes. To address typographical sign errors in Beyer et al. [55], corrected equations are presented in Section 2. Due to the long operational experience with the method, Heliosat-3 is chosen in this study for retrieving GHI from the BRF values of pixels. The improvement in the accuracy of the 15 min resolution Heliosat-3 estimated GHI, by applying correction approach developed in this study, is validated against ground measurements from two Baseline Surface Radiation Network (BSRN) stations and three reference solar irradiance measurement sites of the International Energy Agency's Photovoltaic Power Systems Programme (IEA-PVPS), located in the tropical regions of South and Southeast Asia. Since the clear sky model and atmospheric turbidity data are not changed, any change in accuracy of the estimated GHI occurs solely by applying the corrections on Heliosat-3 CI images. The accuracy of the corrected Heliosat-3 estimated GHI is benchmarked against two openly available datasets: (i) National Solar Radiation Database (NSRDB) [33] and (ii) Copernicus Atmospheric Monitoring Service (CAMS) for solar radiation [58], which provide estimated GHI using images from Meteosat-8 and Himawari-8 and cover the five ground measurement sites used in this study. Given that parallax and cloud shadow displacement effects are expected to become more pronounced in high-resolution imagery from new-generation satellites like Himawari-9, Meteosat Third Generation (MTG), and Geostationary Operational Environmental Satellite (GOES-R), and that these effects are amplified in tropical regions due to the higher tropopause and larger cloud heights, this study makes the following contributions:

1. This study uses a gridded CTH dataset to apply the parallax and cloud shadow shift on individual cloudy pixels in Heliosat-3 CI images with the help of bilinear interpolation, allowing sub-pixel displacements.
2. The reduction in the error of the 15 min resolution satellite estimated GHI, derived from the Heliosat-3 CI images, solely due to applying the parallax and cloud shadow shifts is validated with one year of data from five sites in the tropical region and benchmarked against the existing GHI datasets from NSRDB and CAMS radiation service.
3. Weather situations with particular cloud types are identified for which the largest errors and error reductions are observed after correcting the CI images.
4. The error reduction is found to be dependent on the co-scattering angle (ψ) between the azimuth of the sun (φ) and the satellite (φ_{saa}) with respect to the sites that have sufficient cloud information available on all sides in the vicinity.
5. A minimum threshold value of CTH is found below which no change in error is observed at any of the sites
6. The weather situation in which maximum error reduction occurs shifts from partly cloudy to overcast with the increase in the viewing zenith angle (θ_{sza}) from the satellite.
7. The improvement in GHI ramp estimation after applying the correction is validated with the ramp score metric.

2. Data and method

2.1. Data

2.1.1. Global Horizontal Irradiance from satellite images

This analysis uses the 0.6 μm visible channel images from the geostationary Meteosat-8 satellite, positioned over the Indian Ocean at 41.5°E, for the year 2018. The full-disk images have a nominal spatial resolution of 3 km × 3 km at the SSP and a size of 3712 pixels × 3712 pixels, as shown in Fig. 1. These images are available at a temporal resolution of 15 min. For this study, the full-disk images are cropped to a size of 1200 pixels × 1200 pixels, covering the South and Southeast Asian regions, as shown in Fig. 2a, where the five selected sites are located. The pixel intensity values of the satellite images are converted to Bidirectional Reflectance Factor (BRF), following the method described in EUMETSAT [59], with calibration factors obtained from the image headers. The BRF values are then converted into Cloud Index (CI) and Global Horizontal Irradiance (GHI) using the Heliosat-3 method described in Hammer et al. [60]. Although the Heliosat method was originally developed for broadband High Resolution Visible (HRV) channel images, it has since been applied to the 0.6 μm and 0.8 μm channels [26]. To derive the CI of a pixel (eq. 1), the reference value of the cloud BRF (ρ_c) and the Earth surface BRF (ρ_g) of that pixel are required. ρ_g is estimated individually for each pixel and corresponds to the most frequent low BRF value (5th percentile) from the pixel's time series. ρ_c is estimated for the entire image and corresponds to the most frequent high BRF value (95th percentile of all values of BRF > 0.5) across the time series for all pixels. Both reference values are derived from the past 30 days of images at the same scan start time in UTC. The GHI is then estimated from CI, as shown in eqs. 2 and 3, while the clear sky irradiance GHI_{clear} is obtained with the model from Dumortier et al. [61], incorporating climatological Linke turbidity data from Remund et al. [62].

$$CI = \frac{(\rho - \rho_g)}{(\rho_c - \rho_g)} \tag{1}$$

where,

CI : cloud index of a pixel
ρ : actual BRF value of the pixel
ρ_c : reference BRF of cloud
ρ_g : reference Earth surface BRF for the pixel

$$k_c = 1.2, for\ n \leq -0.2 \tag{2a}$$

$$k_c = 1 - CI, for -0.2 < CI \leq 0.8 \tag{2b}$$

$$k_c = 1.661 - 1.7814CI + 0.7250CI^2, for\ 0.8 < CI \leq 1.05 \tag{2c}$$

$$k_c = 0.09, for\ 1.05 < CI \tag{2d}$$

where,
k_c : clear sky index

$$GHI = k_c \times GHI_{clear} \tag{3}$$

where,

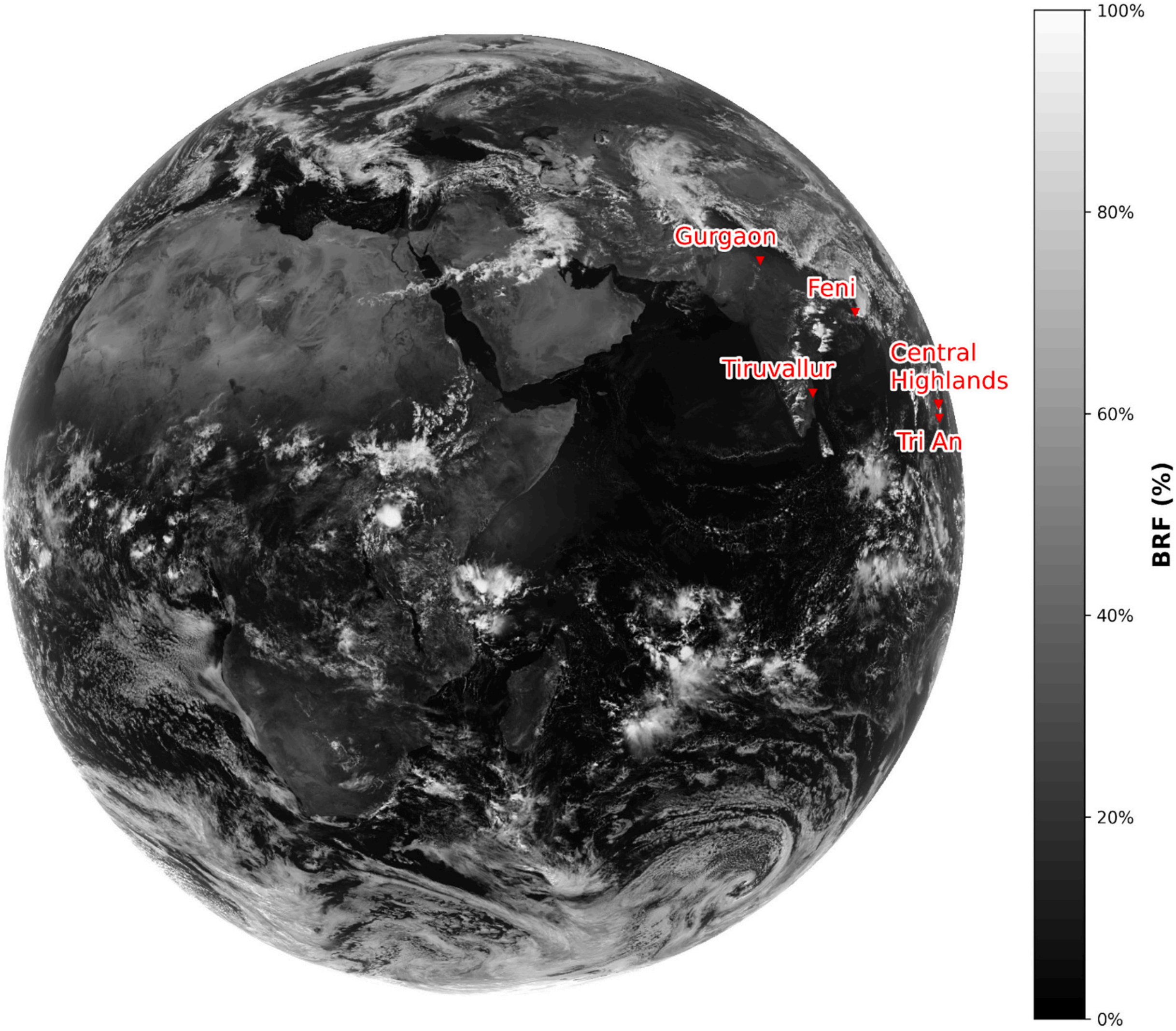

Fig. 1. Full disk Meteosat-8 0.6 μm visible channel image with the locations of the measurement stations

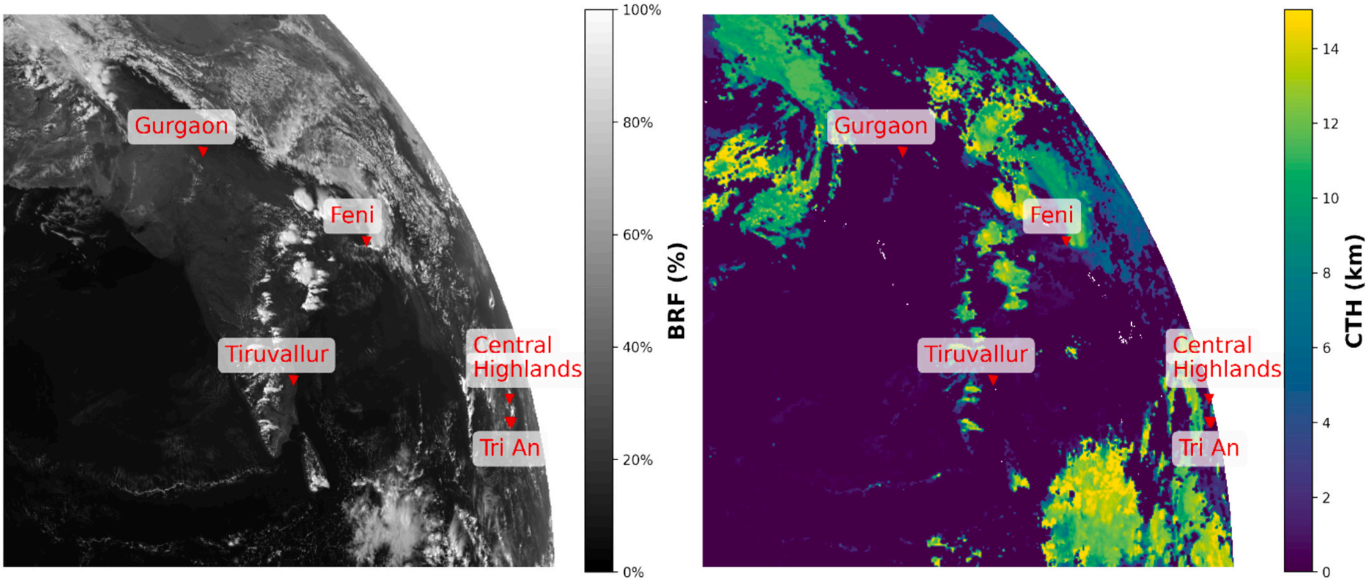

Fig. 2. South Asian section of Meteosat-8 (a) 0.6 μm visible channel image and (b) cloud top height (CTH) image from the EUMETSAT archive.

GHI : satellite estimated GHI
GHI_{clear} : clear sky GHI

2.1.2. Ground measurements

Ground-measured GHI data at 1 min temporal resolution is obtained from two BSRN stations [63,64] and three IEA-PVPS sites [65], as shown in Figs. 1 and 2. All sites are located in regions of South and Southeast Asia affected by the monsoon. The Gurgaon BSRN station is situated in a hot semi-arid (BSh) Köppen-Geiger climate zone of northern India, where the maximum cloudiness due to atmospheric convection occurs during the southwest summer monsoon season (June–September) [15]. Both the Tiruvallur BSRN station and the Central Highlands IEA-PVPS site are located in tropical savanna (Aw) climate zones. While the Central Highlands site only experiences the southwest monsoon [66], the Tiruvallur site is also affected by intense atmospheric convection during the winter northeast monsoon (October–December). The IEA-PVPS sites of Feni and Tri An are located in the tropical monsoon (Am) climate zone and are affected only by the southwest monsoon. The Feni region frequently experiences severe local convective storms, known as Nor'westers, during the pre-summer monsoon period of April–May [23]. The ground-measured GHI datasets from all sites are quality checked using the physical possible limit (PPL) and extremely rare limit (ERL) tests, before averaging to 15 min temporal resolution. As shown in Table 1, the θ_{sza} of the sites from the Meteosat-8 varies between 46° and 76°.

2.1.3. Datasets from NSRDB and CAMS radiation service

GHI time series data at 15 min temporal resolution, derived from Meteosat-8 using the Physical Solar Model (PSM) v3, are obtained from the NSRDB for the Gurgaon, Tiruvallur and Feni sites [33]. For the Tri An and Central Highlands sites, the PSM v3 GHI time series data, derived from Himawari-8 at the native 10 min resolution, are also obtained from the NSRDB. Additionally, PSM v3 cloud type time series data, derived from Meteosat-8 at 15 min resolution or from Himawari-8 at 10 min resolution (depending on data availability) is retrieved for all pixel coordinates in a 21 × 21 pixels grid surrounding the location of the five sites in the 0.6 μm Meteosat-8 visible channel image. The cloud type classification is based on the Clouds from AVHRR Extended System (CLAVR-x) processing system, the latest iteration of several CLAVR algorithms ([67],[68]), which is used for generating quantitative cloud products in real time. In addition, GHI estimated from Himawari-8 images using the Heliosat-4 method at 15 min resolution is obtained for the Tri An and Central Highlands sites from the CAMS radiation service [69].

2.1.4. Cloud top height

The CTH dataset for the year 2018 is obtained from the Meteorological Products Extraction Facility (MPEF) algorithm. This dataset provides the height of the highest cloud within a superpixel of 3 × 3 pixels in the 0.6 μm visible channel images, with a vertical resolution of 300 m. In the MPEF algorithm, the cloud top pressure level (in hPa) is estimated using data from the MSG 6.2 μm water vapour (WV) channel, 7.3 μm WV channel, 10.8 μm IR channel and 13.4 μm IR channel. However, the algorithm tends to underestimate cloud top pressure, with an uncertainty as high as 150 hPa for liquid clouds [70]. The CTH height in meters is then derived by interpolating the vertical standard atmospheric profile from the International Civil Aviation Organization (ICAO) to the estimated cloud top pressure level ([71],[72]). However, it must be noted that in unstable atmospheric situations, the real profile may differ significantly from the standard profile. Moreover, the retrieval of multiple cloud layer heights is not possible, as lower cloud layers are concealed by upper layers. The full-disk CTH images have a coarser resolution and a reduced image size of 1237 pixels × 1237 pixels. These images are upscaled to 3712 × 3712 pixels—the size of the 0.6 μm visible channel image—by bilinear interpolation of the CTH values, followed by smoothing with a Gaussian filter with a kernel size of 7. Finally, the images are cropped to 1200 pixels × 1200 pixels to cover the South and Southeast Asian region, as shown in Fig. 2b.

2.2. Methods

2.2.1. Parallax correction

Cloudy pixels in CI images are displaced from their actual positions. This displacement depends on the CTH above the surface, as well as the satellite viewing zenith angle (θ_{sza}) and azimuth angle (φ_{saa}) of the cloudy pixel, as illustrated in Fig. 3. The angles θ_{sza} and φ_{saa} are calculated using eqs. 4 and 5, assuming positive values for longitudes to the east and latitudes to the north. The mean height above the Earth's surface ($H_{sat} = 35786km$) and the satellite's position ($Lon^{sat} = 41.5^{\circ}E$) are used for these calculations [73,74]. The Earth's radius (R) is assumed to be 6378.140 km [75]. The longitude Lon^{pixel} and latitude Lat^{pixel} coordinates for the apparent location (A) of each cloudy pixel are obtained from the satellite's latitude-longitude grid, which provides the center coordinates of each pixel. The cloud parallax displacement between the apparent location (A) and the actual location (B) is estimated using eqs. 6(a) and 6(c). The displacements are subtracted from Lon^{pixel} and Lat^{pixel} to obtain the parallax corrected longitude ($Lon^{pix}_{parallax\_corrected}$) and latitude ($Lat^{pix}_{parallax\_corrected}$), as shown in eqs. 6(b) and 6(d). This correction is applied to every cloudy pixel with a CTH greater than 0. Fig. 4 summarizes the parallax correction process in the form of a flowchart.

$$\varphi^{pix}_{saa} = tan^{-1}\left(\frac{tan\left(\left|Lon^{sat} - Lon^{pix}\right|\right)}{sin\left(Lat^{pix}\right)}\right), if Lon^{pix} > Lon^{sat} and Lat^{pix} > 0^{\circ} \tag{4a}$$

$$\varphi^{pix}_{saa} = 180^{\circ} + tan^{-1}\left(\frac{tan\left(\left|Lon^{sat} - Lon^{pix}\right|\right)}{sin\left(Lat^{pix}\right)}\right), if Lon^{pix} > Lon^{sat} and Lat^{pix} < 0^{\circ} \tag{4b}$$

Table 1
Descriptive statistics for the five ground measurement stations.

Site	Location	Climate type	Viewing zenith angle (θ_{sza}) from Meteosat-8	Viewing azimuth angle (φ_{saa}) from Meteosat-8	Viewing zenith angle (θ_{sza}) from Himawari-8	Viewing azimuth angle (φ_{saa}) from Himawari-8	Day time data points after Quality Check	Average Daytime Irradiance (W/m^2)
Gurgaon	28.42°N, 77.16°E	BSh	51.12°	56.44°	74.65°	283.72°	9905	354.1
Tiruvallur	13.09°N, 79.97°E	Aw	46.59°	74.09°	68.96°	277.44°	9016	418.7
Feni	22.80°N, 91.36°E	Am	61.11°	71.90°	59.96°	288.84°	10,266	372.4
Central Highlands	12.75°N, 107.88°E	Aw	75.37°	84.48°	39.85°	289.37°	10,211	428.4
Tri An	11.10°N, 107.04°E	Am	74.35°	84.99°	40.16°	286.54°	10,225	428.2

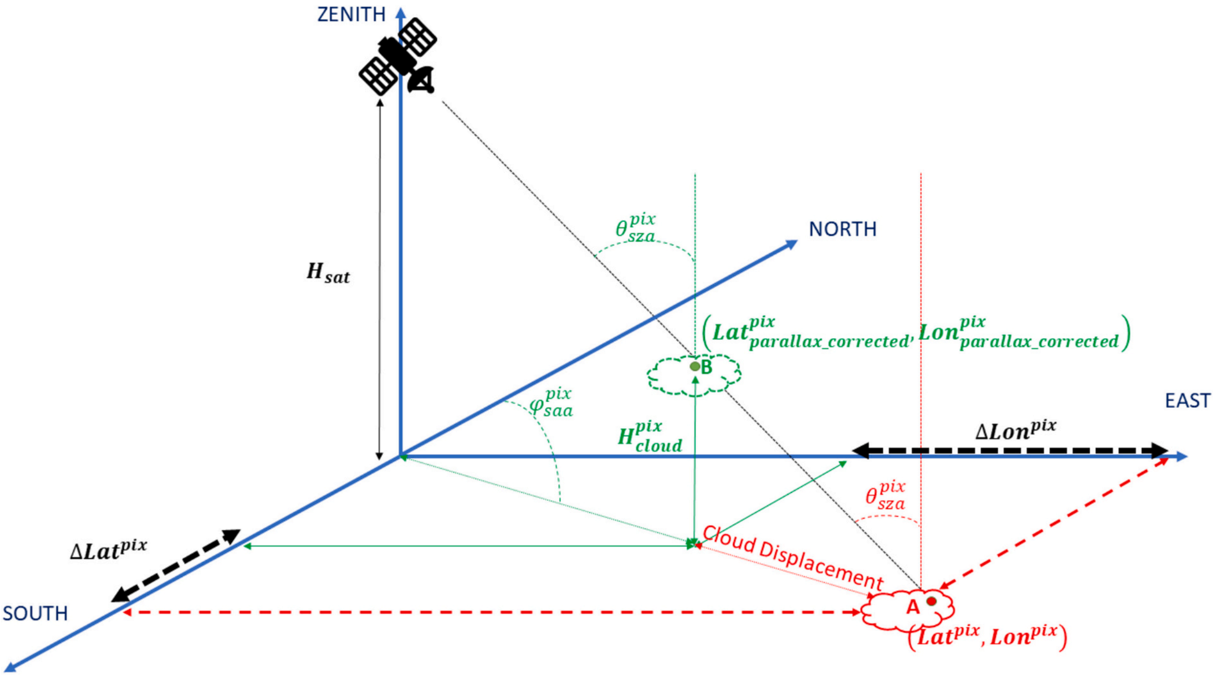

Fig. 3. Schematic representation of the satellite viewing parallax.

$$\varphi_{saa}^{pix} = 180^{\circ} - tan^{-1}\left(\frac{tan\left(\left|Lon^{sat} - Lon^{pix}\right|\right)}{sin\left(Lat^{pix}\right)}\right), if Lon^{pix} < Lon^{sat} and Lat^{pix} < 0^{\circ} \tag{4c}$$

$$\varphi_{saa}^{pix} = 360^{\circ} - tan^{-1}\left(\frac{tan\left(\left|Lon^{sat} - Lon^{pix}\right|\right)}{sin\left(Lat^{pix}\right)}\right), if Lon^{pix} < Lon^{sat} and Lat^{pix} > 0^{\circ} \tag{4d}$$

where,

φ_{saa}^{pix} : azimuth angle of a cloudy pixel when viewed from the satellite
Lon^{sat} : sub satellite longitude
Lon^{pix} : longitude of the cloudy pixel
Lat^{pix} : latitude of the cloudy pixel

$$\theta_{sza}^{pix} = 90^{\circ} - cos^{-1}\left(\frac{H \times \left(sin\left(cos^{-1}\left(cos\left(Lat^{pix}\right) \times cos\left(\left|Lon^{pix} - Lon^{sat}\right|\right)\right)\right)\right)}{\sqrt{R^2 + H^2 - 2 \times R \times H \times cos\left(Lat^{pix}\right) \times cos\left(\left|Lon^{pix} - Lon^{sat}\right|\right)}}\right) \tag{5}$$

where,

θ_{sza}^{pix} : zenith angle of the cloudy pixel when viewed from the satellite
R : radius of the Earth (6378.140 km)
H_{sat} : mean height of the satellite from the Earth surface
$H = R + H_{sat}$: mean height of the satellite from the Earth's center

$$\Delta\left(Lon_{parallax}^{pix}\right) = \frac{H_{cloud}^{pix} \times tan\theta_{sza}^{pix} \times sin\varphi_{saa}^{pix}}{\pi R} \times 180^{\circ} \tag{6a}$$

$$Lon_{parallax\_corrected}^{pix} = Lon^{pix} - \Delta\left(Lon_{parallax}^{pix}\right) \tag{6b}$$

$$\Delta\left(Lat_{parallax}^{pix}\right) = \frac{H_{cloud}^{pix} \times tan\theta_{sza}^{pix} \times cos\varphi_{saa}^{pix}}{\pi R} \times 180^{\circ} \tag{6c}$$

$$Lat_{parallax\_corrected}^{pix} = Lat^{pix} - \Delta\left(Lon_{parallax}^{pix}\right) \tag{6d}$$

where,

H_{cloud}^{pix} : height of the cloud top from the Earth surface in the pixel
$\Delta\left(Lon_{parallax}^{pix}\right)$: shift in the longitude of the cloudy pixel due to parallax
$Lon_{parallax\_corrected}^{pix}$: parallax corrected longitude of the cloudy pixel
$\Delta\left(Lat_{parallax}^{pix}\right)$: shift in the latitude of the cloudy pixel due to parallax
$Lat_{parallax\_corrected}^{pix}$: parallax corrected latitude of the cloudy pixel

2.2.2. *Cloud shadow projection*

A cloud's shadow is not directly beneath the cloud unless the sun is positioned exactly at the zenith. The actual location of the shadow shifts throughout the day. The displacement depends on the CTH and the solar zenith (θ_z) and azimuth (φ) angles, as illustrated in Fig. 5. The angles θ_z and φ are calculated using the Solar Geometry 2 (sg2) algorithms [76]. The shadow's displacement from the parallax corrected cloud location is then estimated using eqs. 7(a) and 7(c) for longitude and latitude respectively, for each cloudy pixel. The CI values are assigned to the projected shadow coordinates, as obtained from eqs. 7(b) and 7(d). Assigning the projected shadow CI values to the nearest satellite latitude-longitude grid point results in whole-pixel displacements. However, by calculating the exact displacement in latitude and longitude, and then bilinearly interpolating back to the original satellite grid, fractional pixel shifts are accounted for. The entire procedure is summarized in the form of a flowchart in Fig. 6.

$$\Delta\left(Lon_{shadow}^{pix}\right) = \frac{H_{cloud}^{pix} \times tan\theta_{z}^{pix} \times sin\varphi^{pix}}{\pi R} \times 180^{\circ} \tag{7a}$$

$$Lon_{shadow}^{pix} = Lon_{parallax\_corrected}^{pix} - \Delta\left(Lon_{shadow}^{pix}\right) \tag{7b}$$

$$\Delta\left(Lat_{shadow}^{pix}\right) = \frac{H_{cloud}^{pix} \times tan\theta_{z}^{pix} \times cos\varphi^{pix}}{\pi R} \times 180^{\circ} \tag{7c}$$

$$Lat_{shadow}^{pix} = Lat_{parallax\_corrected}^{pix} - \Delta\left(Lat_{shadow}^{pix}\right) \tag{7d}$$

where,

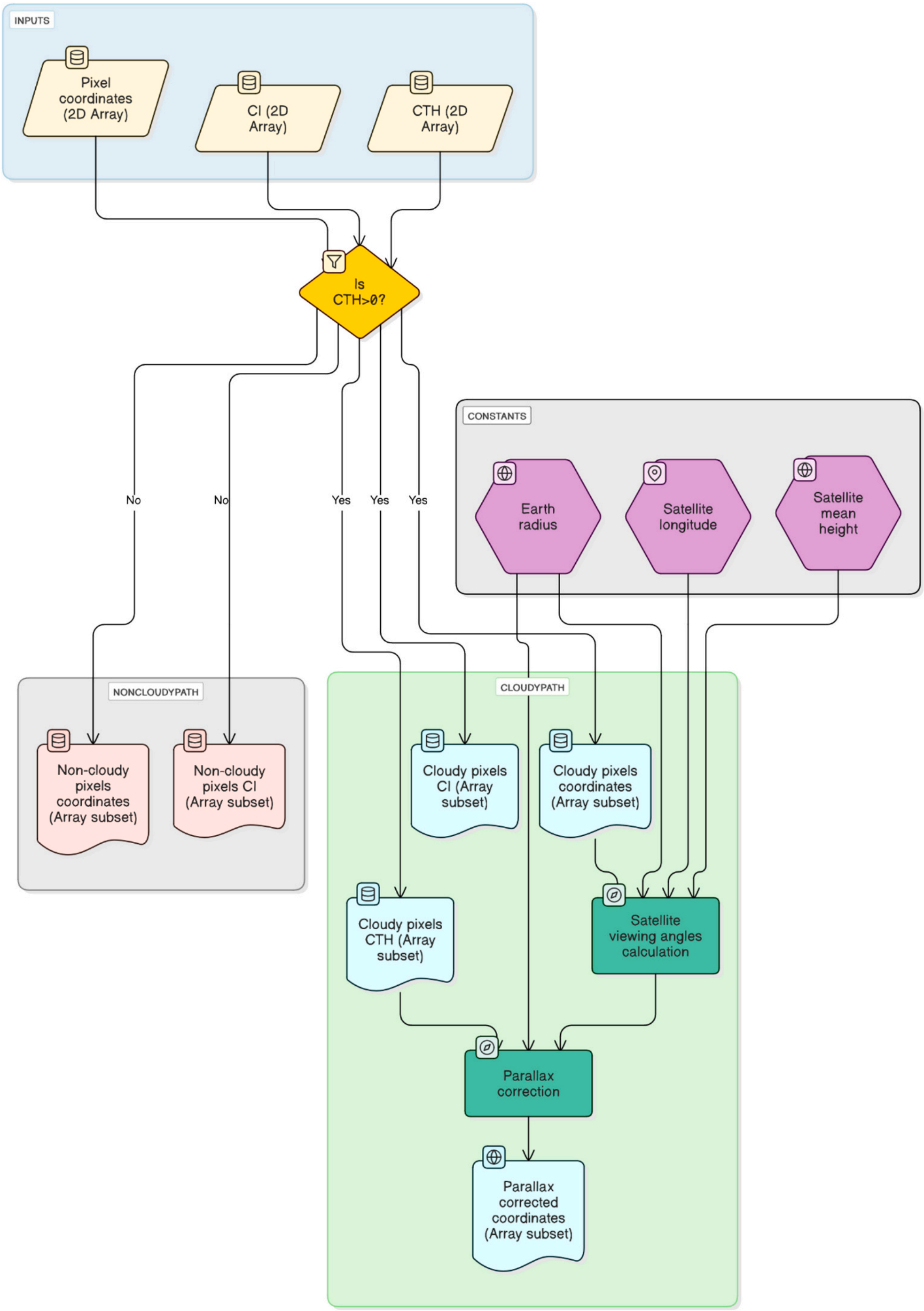

Fig. 4. Parallax correction procedure.

θ_z^{pix} : zenith angle of the sun with respect to the cloudy pixel

φ^{pix} : azimuth angle of the sun with respect to the cloudy pixel

$\Delta\left(Lon_{shadow}^{pix}\right)$: shift in the longitude of the shadow from the cloudy pixel

Lon_{shadow}^{pix} : longitude of the shadow due to the cloudy pixel

$\Delta\left(Lat_{parallax}^{pix}\right)$: shift in the latitude of the cloudy pixel due to parallax

Lat_{shadow}^{pix} : latitude of the shadow due to the cloudy pixel

2.2.3. Pixel-by-pixel processing

In the method introduced by Beyer et al. [55], cloud shadow displacement was applied to the CI images using only whole-pixel shifts. The CTH, along with the sun and satellite viewing geometry, was used to estimate the geometric displacement of a cloud's shadow. However, the resulting displacements were applied in discrete steps by reassigning the CI value to the nearest satellite pixel – i.e., to the center coordinates of the closest grid cell. This effectively neglected sub-pixel shifts, leading to abrupt transitions and potential loss of spatial detail in the corrected CI image.

The method proposed by Miller et al. [56] addressed the difficulty of tracking individual cloudy pixels by grouping adjacent cloudy pixels into cloud objects based on spatial connectivity and similarity in retrieved cloud properties. All pixel in a cloud object were then assigned the same CTH and cloud properties, which were then used for computing parallax correction and shadow projection. While this grouping strategy

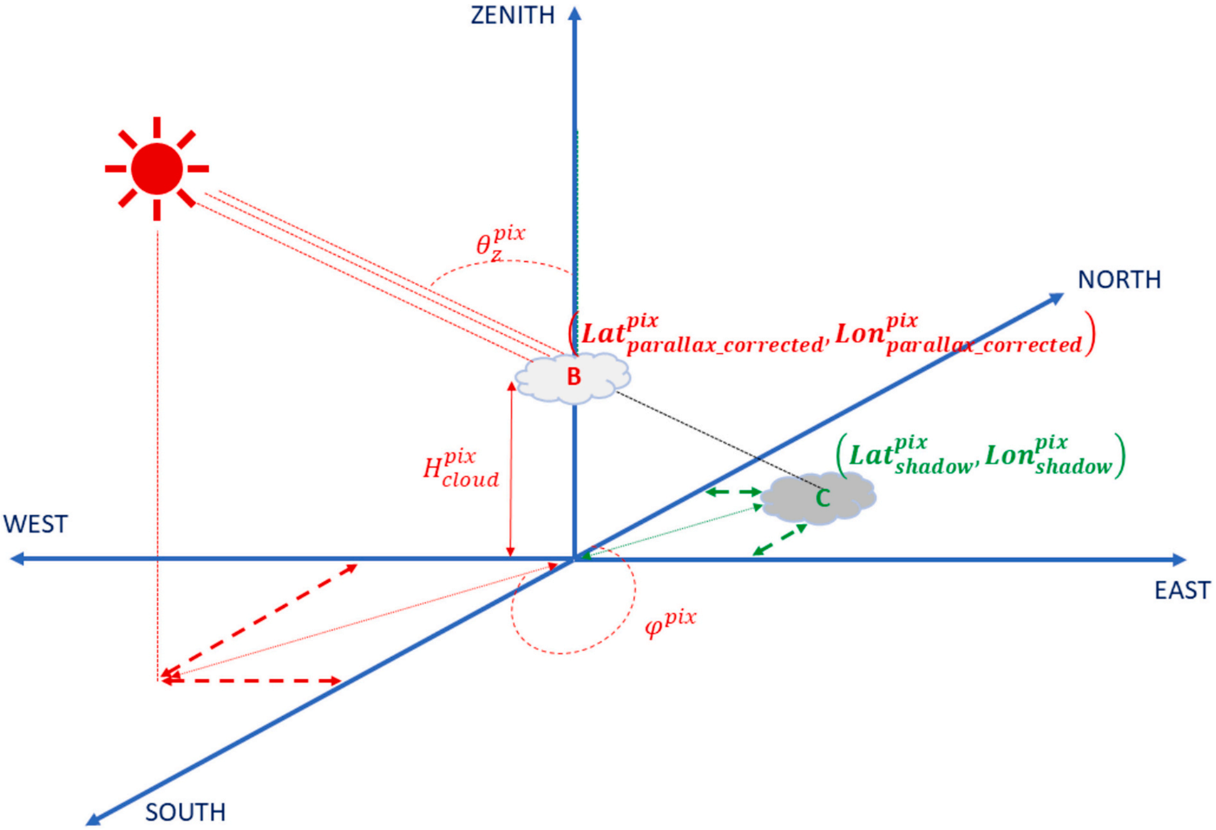

Fig. 5. Schematic representation of the cloud shadow projection on the ground.

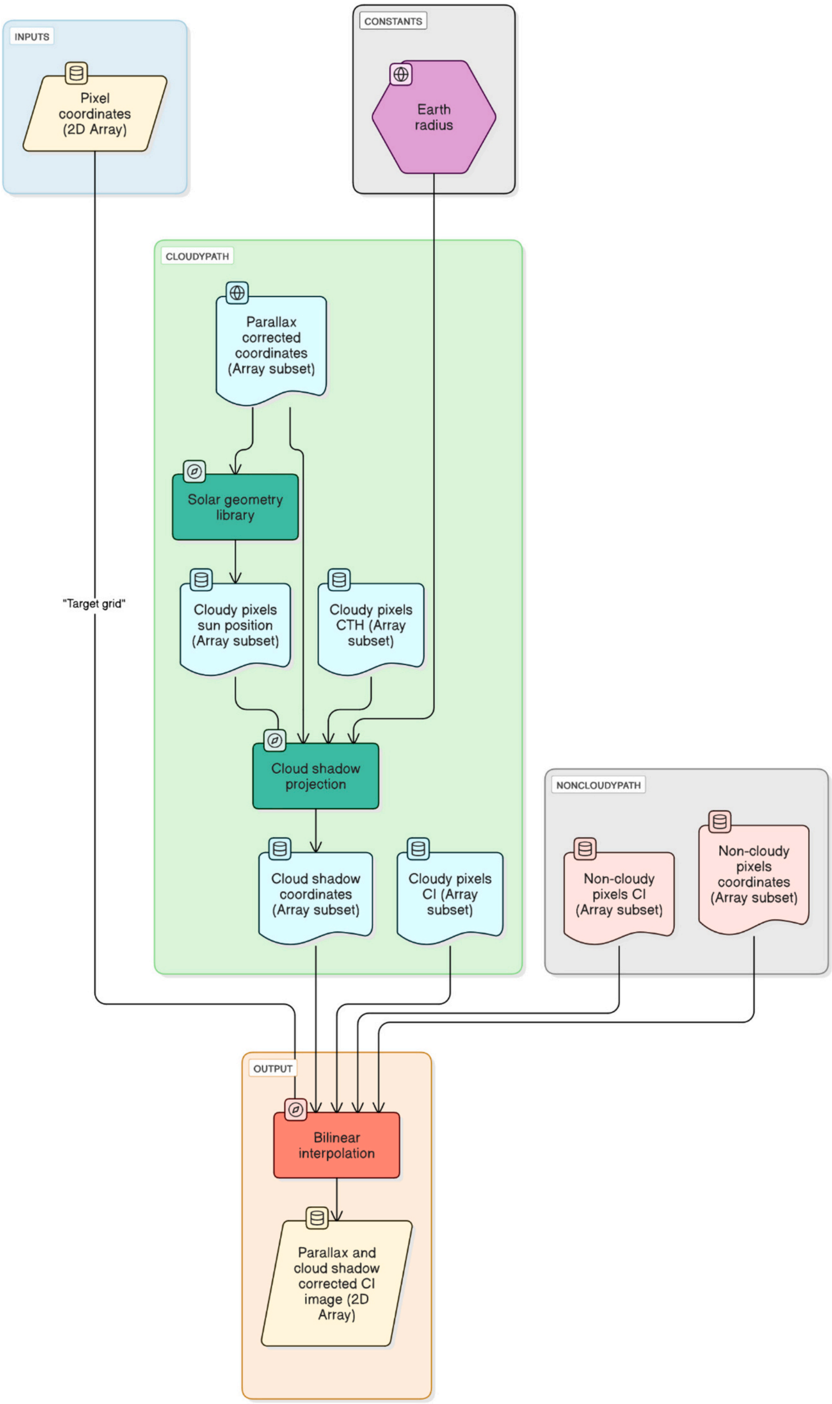

Fig. 6. Cloud shadow projection procedure.

reduced computational complexity by applying the same parallax and shadow displacement to all pixels within a cloud object uniformly, it introduced smoothing effects that could obscure variations in cloud shadow geometry for heterogeneous cloud fields.

In contrast, the method presented in this study performs pixel-level corrections by retaining the exact displaced shadow coordinates for each cloudy pixel, based on its specific CTH, satellite viewing geometry and solar position. These shadow coordinates often do not coincide with the satellite pixel center coordinates and form a scattered set of sub-pixel positions. To estimate the CI value at any defined query point (such as a satellite pixel center or a ground station location), Delaunay triangulation is applied to the displaced shadow coordinates, followed by barycentric bilinear interpolation. This approach produces a weighted average of the surrounding Delaunay triangle vertices and effectively captures partial pixel contributions without hard assignment to the nearest pixel. This preserves spatial details and makes the method well-suited for complex cloud scenarios.

For each image sub-section of size 1200 × 1200 pixels, the entire parallax and cloud shadow displacement calculation along with the bilinear interpolation requires 10–15 s, depending on the number of cloudy pixels in the image scene. This time latency is negligible compared to the image update interval of modern geostationary satellites, which ranges from 10 to 15 min. Consequently, this approach could be easily integrated into operational solar forecasting systems without any significant latency issues.

2.2.4. Evaluation technique

The Heliosat-3 estimated GHI is validated against the ground-measured GHI described in Section 2.1.2, before and after the applying the corrections with the method described in Sections 2.2.1 and 2.2.2. Only daytime values – timestamps where the ground-measured GHI exceeds 0 W/m^2 – are used to compute error metrics such as RMSE, MAPE (mean absolute percentage error), mean absolute error (MAE) and ramp score (eqs. 8, 11, 12 and 14). The relative error metrics for any period are calculated by normalizing with the average of the daytime measured GHI in that period.

$$RMSE_{monthm} = \sqrt{\frac{1}{N}\sum_{monthm}\left(GHI_{estim} - GHI_{meas}\right)^2} \tag{8}$$

where,

$RMSE_{month\ m}$: root mean square error in uncorrected or corrected Heliosat-3 estimated GHI for any month m

N : total number of quality controlled daytime datapoints in month m

GHI_{estim} : Uncorrected or corrected Heliosat-3estimated GHI at 15 min resolution

GHI_{meas} : ground-measured GHI at 15 min resolution

To analyze the effect of sun-site-satellite geometry across different seasons, the datasets for each site are divided into pre-noon ($\varphi < 180^\circ$) and post-noon ($\varphi > 180^\circ$) periods for each month. The change in monthly RMSE after applying the parallax and shadow corrections is calculated separately for the pre-noon and post-noon periods, as described in eq. 9.

$$\Delta RMSE\%_{month\ m} = \frac{RMSE^{uncorrected}_{month\ m} - RMSE^{corrected}_{month\ m}}{\left(\frac{\sum_{monthm} GHI_{meas}}{N}\right)} \times 100 \tag{9}$$

where,

$\Delta RMSE\%_{month\ m}$: percentage change in RMSE after performing parallax correction or parallax and shadow correction for any month m

$RMSE^{uncorrected}_{month\ m}$: RMSE in satellite estimated GHI for any month m when no corrections are applied

$RMSE^{corrected}_{month\ m}$: RMSE in satellite estimated GHI for any month m after applying parallax correction or parallax and cloud shadow correction

Table 2

R^2 between the satellite estimated GHI and the ground measured GHI at 15 min resolution* for the year 2018.

Site	Uncorrected Heliosat-3 GHI	Parallax and Shadow corrected Heliosat-3 GHI
Gurgaon	0.91	0.93
Tiruvallur	0.93	0.94
Feni	0.88	0.90
Central Highlands	0.81	0.83
Tri An	0.82	0.85

* Only the valid daytime datapoints mentioned in Table 1

The reduction in the MAE of the Heliosat-3 estimated GHI after applying the corrections is calculated based on the sun's varying θ_z and φ in 10° and 15° bins respectively, as shown in eq. 10.

$$\Delta MAE_{\left[\theta_z^1-\theta_z^2,\ \varphi^1-\varphi^2\right]} = \frac{1}{N}\cdot\sum_{\left[\theta_z^1-\theta_z^2,\ \varphi^1-\varphi^2\right]}\left|GHI^{uncorr}_{estim} - GHI_{meas}\right| - \frac{1}{N}\cdot\sum_{\left[\theta_z^1-\theta_z^2,\ \varphi^1-\varphi^2\right]}\left|GHI^{corr}_{estim} - GHI_{meas}\right| \tag{10}$$

where,

$\Delta MAE_{\theta_z^1-\theta_z^2,\varphi^1-\varphi^2}$: reduction or increase in MAE when the solar zenith angle is within $\theta_z^1 - \theta_z^2$ and the azimuth angle is between $\varphi^1 - \varphi^2$ in W/m^2

GHI^{uncorr}_{estim} : Uncorrected Heliosat-3 estimated GHI at 15 min resolution

GHI^{corr}_{estim} : Corrected Heliosat-3 estimated GHI at 15 min resolution

To examine the performance variation with cloud height, the binned MAPE is computed using eq. 11 at CTH ranges of 0–2 km, 2–4 km, 4–6 km, 6–8 km, 8–10 km, 10–12 km, 12–14 km and 14–16 km. The GHI at a site can be influenced not only by clouds directly overhead but also by clouds elsewhere in the sky dome, depending on the sun's position. To account for all clouds that may cast shadows at a site, especially during low solar elevation angles, the CTH is spatially averaged across 21 pixel × 21 pixel area (= 63 km × 63 km) surrounding the ground measurement stations.

$$MAPE_{[h_1-h_2]} = \frac{1}{N}\cdot\sum_{[h_1-h_2]}\frac{\left|GHI_{estim} - GHI_{meas}\right|}{GHI_{meas}} \tag{11}$$

where,

$MAPE_{[h_1-h_2]}$: Mean absolute percentage error in satellite estimated GHI when the average CTH in a 21 × 21 pixels area around the site lies between h_1 and h_2

Datapoints are binned based on their $\boldsymbol{k_c}$ values, grouped into bins of 0.1 interval across the [0,1] range. The binned average MAE is then calculated for each $\boldsymbol{k_c}$ group, as shown in eq. 12.

$$MAE_{\left[k_c^1-k_c^2\right]} = \frac{1}{N}\cdot\sum_{\left[k_c^1-k_c^2\right]}\left|GHI_{estim} - GHI_{meas}\right| \tag{12}$$

where,

$MAE_{\left[k_c^1-k_c^2\right]}$: Mean Absolute Error in satellite estimated GHI when the ground measured clear sky index lies between k_c^1 and k_c^2

The percentage of cloudy pixels belonging to each CLAVR-X cloud type in a 21 × 21 pixels box around each site is computed to assess the dependency of the error and correction on cloud type.

The accuracy of satellite-estimated GHI ramps is evaluated using the ramp score metric introduced by Vallance et al. [14]. Individual GHI ramps for each day are identified in both the satellite estimates and the ground measurements using the Swinging Door Algorithm (SDA), originally published in [77], with a ramp threshold ($\Delta GHI_{rampthresh}$) that varies based on the daily maximum of the clear sky GHI, as shown in eq. 13.

Table 3

Rel. RMSE in satellite estimated GHI at 15 min resolution from different models for the year 2018*

Site	Heliosat-3 Meteosat-8	Heliosat-3 Meteosat-8 with Parallax and Shadow Correction	NSRDB Meteosat-8	NSRDB Himawari-8	CAMS Himawari-8
Gurgaon	17.1 %	15.5 %	19.8 %	Not Available	Not Available
Tiruvallur	13.8 %	12.8 %	16.9 %	Not Available	Not Available
Feni	26.3 %	24.4 %	31.4 %	34.6 %	26.9 %
Central Highlands	32.4 %	30.1 %	Not Available	29.0 %	26.1 %
Tri An	31.3 %	29.3 %	Not Available	27.7 %	24.8 %

* Only the valid daytime datapoints mentioned in Table 1

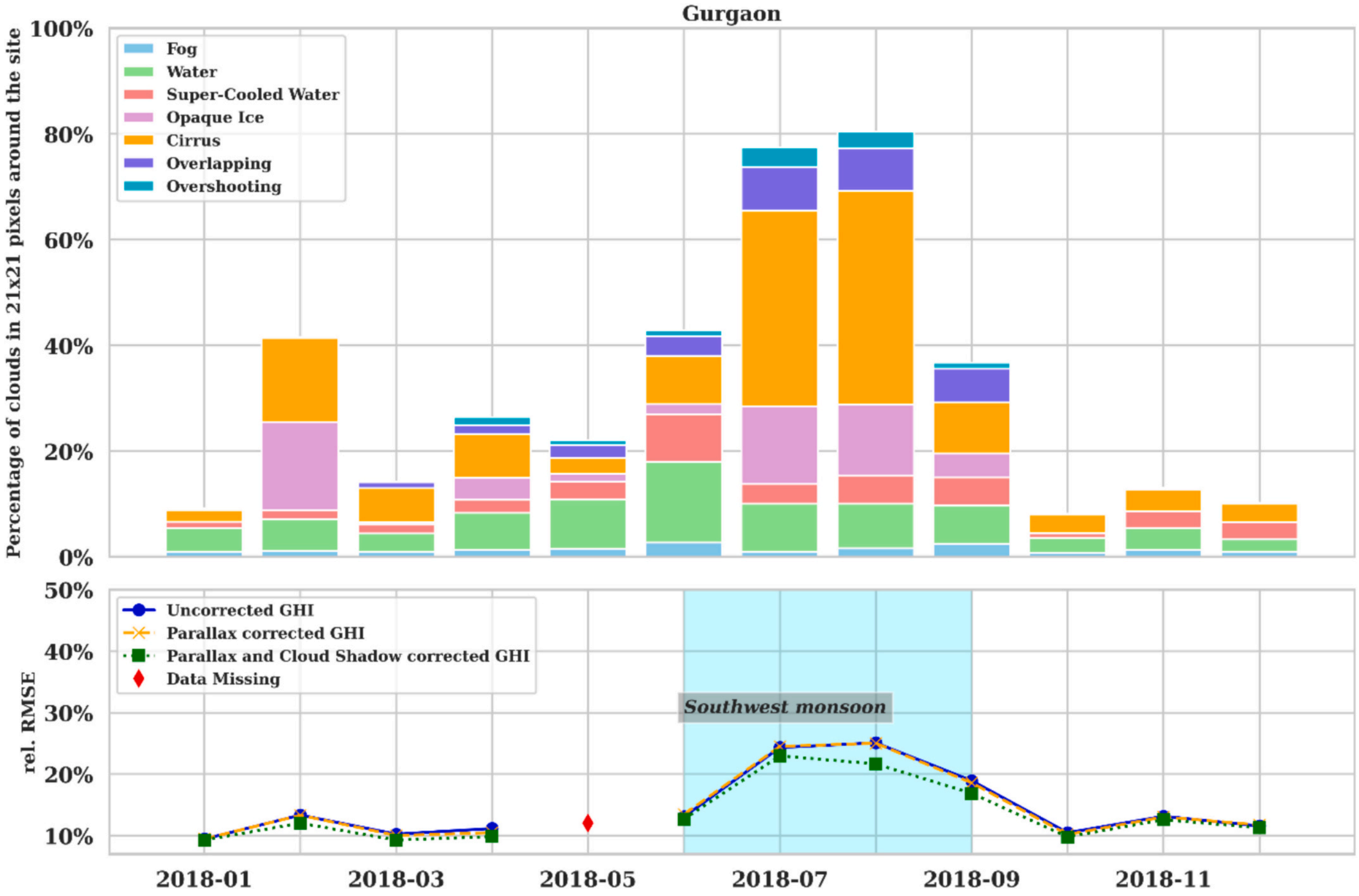

Fig. 7. (a) Percentage of cloudy pixels according to CLAVR-X cloud type retrieved from 21 × 21 pixels of Meteosat-8 image around the site (b) monthly rel. RMSE in 15 min resolution Heliosat-3 estimated GHI at the Gurgaon site.

$$\Delta GHI_{thresh,T_i} = \tau.\max_{\substack{day\ D\\ T_j\in D}}\left(GHI_{clearsky,T_j}\right) for\ T_i \in D \qquad (13)$$

where,

$\Delta GHI_{thresh,T_i}$: The minimum change in GHI above which ramps are detected at time T_i on the Dth day of the year

τ: A value within (0,1) representing a fraction of the maximum clear sky GHI

$GHI_{clearsky,T_j}$: Clear sky GHI at any time T_j on the day of the year D

Hourly normalized ramps, in W.m^{-2}.h^{-1}, are computed from the detected ramp-up or ramp-down points in both the satellite-estimated and ground-measured GHI using the SDA algorithm. The ramp score metrics for both the uncorrected and corrected satellite-estimated GHI are then determined with eq. 14.

$$RS = \frac{1}{t_{max} - t_{min}} \int_{t_{min}}^{t_{max}} \left| ramp_{sat,T_i} - ramp_{ground,T_i} \right| dt \qquad (14)$$

t_{min}: Beginning of the time period of analysis
t_{max}: End of the time period of analysis

3. Results and discussions

3.1. Validation of error reduction and benchmark against NSRDB and CAMS radiation service

As shown in Table 2, the coefficient of determination (R^2) between the 15 min resolution Heliosat-3 estimated GHI and the ground measured GHI at each site increases after applying the corrections to the CI images. The number of datapoints used for this analysis is provided in Table 1. Notably, R^2 values, both before and after corrections, decrease monotonically as the θ_{sza} increases. After applying the parallax and cloud shadow displacement corrections to the CI images from Meteosat-8, the rel. RMSE in the 15 min resolution Heliosat-3 estimated GHI decreases by 1.0, 1.6, 1.9, 2.1 and 2.2 percentage points at Tiruvallur, Gurgaon, Feni, Tri An and Central Highlands respectively (see Table 3). This pattern corresponds to the increase in θ_{sza} of Meteosat-8 from

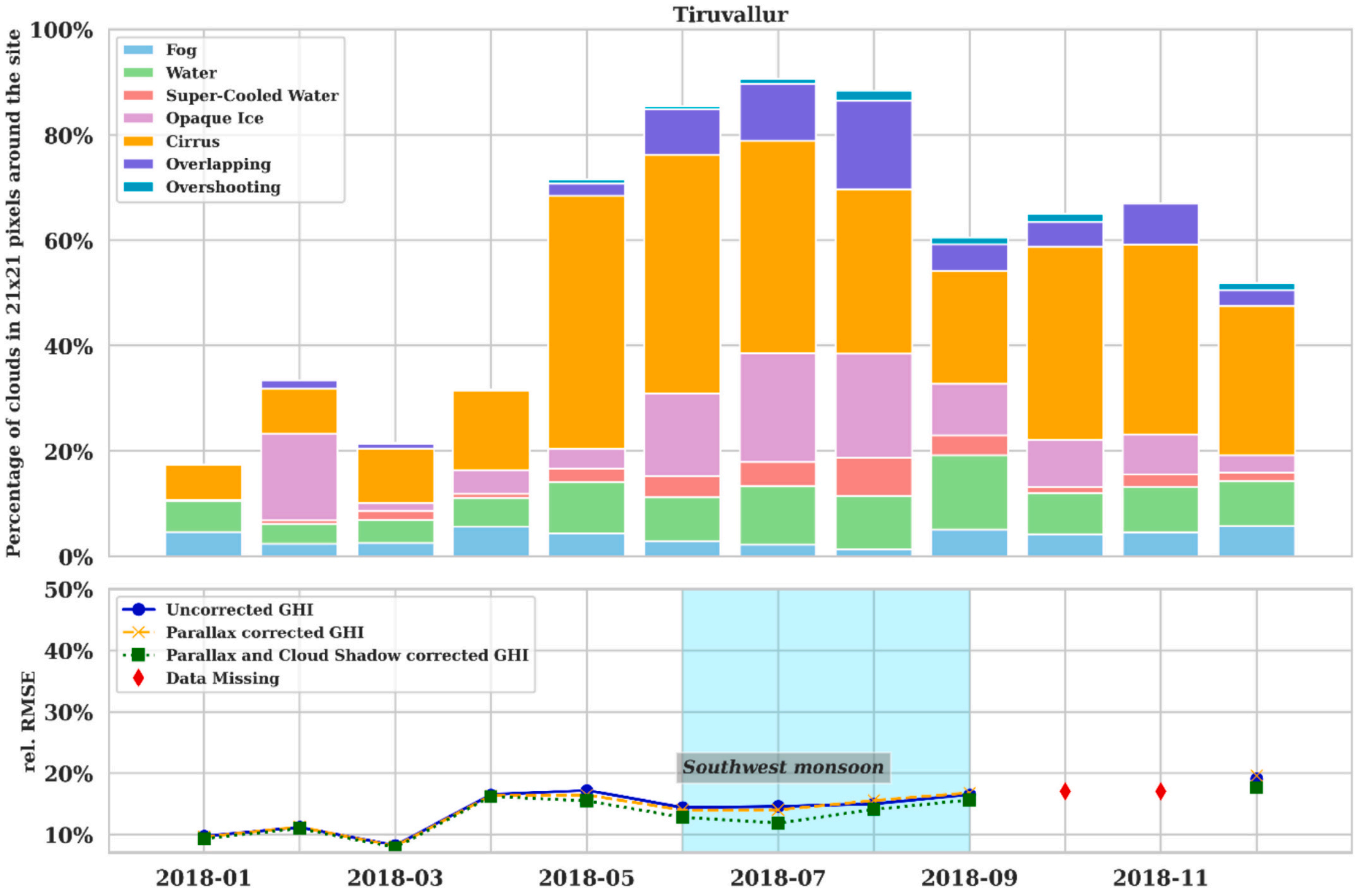

Fig. 8. (a) Percentage of cloudy pixels according to CLAVR-X cloud type retrieved from 21 × 21 pixels of Meteosat-8 image around the site (b) monthly rel. RMSE in 15 min resolution Heliosat-3 estimated GHI at the Tiruvallur site.

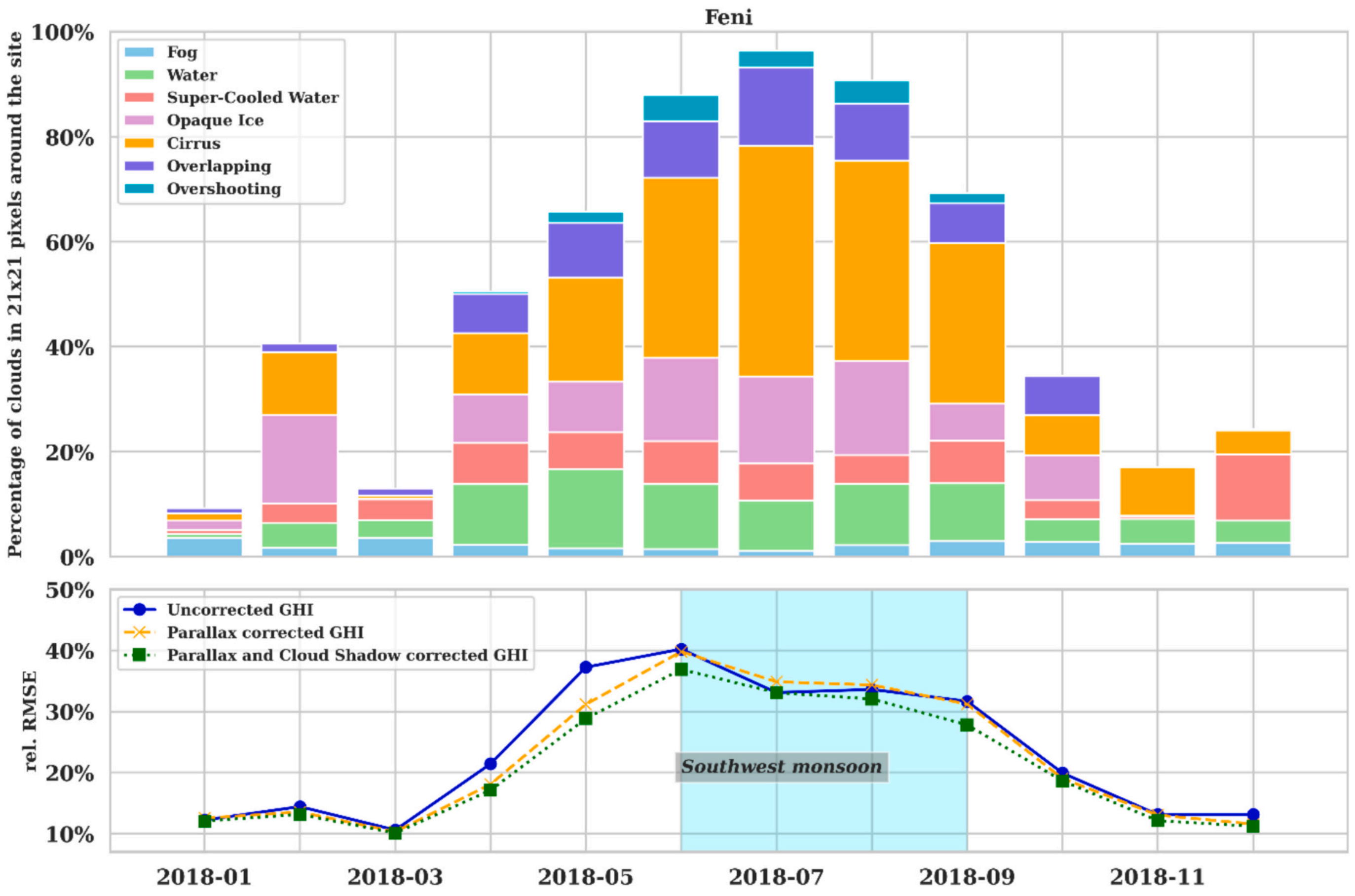

Fig. 9. (a) Percentage of cloudy pixels according to CLAVR-X cloud type retrieved from 21 × 21 pixels of Meteosat-8 image around the site (b) monthly rel. RMSE in 15 min resolution Heliosat-3 estimated GHI at the Feni site.

Tiruvallur to Central Highlands, as shown in table 1.

Bieliński [53] validated the improvement in satellite estimated cloud optical thickness (COT) by applying parallax correction, using radar reflectance measurements. The study demonstrated that parallax correction increased the Pearson's correlation between satellite-estimated COT and radar reflectance from 0.556 to 0.683. However, the authors did not perform cloud shadow projection or validate the improvement in GHI. Lorenzo et al. [50] employed an optimal interpolation approach that reduced the RMSE of estimated GHI from 98.8 W/m^2 to 71.1 W/m^2 for the UASIBS model and from 140 W/m^2 to 72.7 W/m^2 for the SUNY model, when validated against four months of ground-measured GHI data from 22 stations. While this approach included corrections for cloud shadow geolocation, the specific reduction in error due to this correction was not quantified. Miller et al. [56] took a different approach, grouping adjacent cloudy pixels into a single cloud object before applying parallax and cloud shadow corrections. Their one-hour-ahead forecast was validated against two years of ground-measured GHI from four stations, with RMSE values ranging from 120 W/m^2 to 200 W/m^2. However, they did not isolate or validate the impact of parallax and cloud shadow corrections on GHI accuracy. In this study, we benchmarked the reduction of the rel. RMSE in Heliosat-3 estimated GHI at 15 min resolution over one year. After applying the corrections, the rel. RMSE in GHI estimates decreased from 60 W/m^2 (17.1 %) to 55 W/m^2 (15.5 %) at Gurgaon, from 58 W/m^2 (13.8 %) to 54 W/m^2 (12.8 %) at Tiruvallur, from 97.9 W/m^2 (26.3 %) to 90.8 W/m^2 (24.4 %) at Feni, from 138.2 W/m^2 (32.3 %) to 129.1 W/m^2 (30.1 %) at Central Highlands and from 134.1 W/m^2 (31.3 %) to 125.3 W/m^2 (29.3 %) at Tri An.

The GHI estimated from Meteosat-8 images at 15 min resolution using the Heliosat-3 model shows 2.7 and 3.1 percentage points lower rel. RMSE at Gurgaon and Tiruvallur, respectively, compared to GHI estimates from NSRDB, which also uses Meteosat-8 images with similar θ_{sza} over a one-year period (see Table 3). After applying the parallax and cloud shadow corrections, Heliosat-3 estimated GHI shows an even greater improvement, with 4.3 and 4.1 percentage points less rel. RMSE than NSRDB at the two sites. For Feni, which has almost the same θ_{sza} from both Meteosat-8 and Himawari-8 (see Table 1), the uncorrected Heliosat-3 estimated GHI from Meteosat-8 images has 5.1, 8.3, and 0.6 percentage points less rel. RMSE compared to GHI estimates from NSRDB Meteosat-8, NSRDB Himawari-8, and CAMS Himawari-8, respectively. After applying the corrections, the differences in rel. RMSE further increase to 7, 10.2, and 2.5 percentage points. At Tri An and Central Highlands, where the θ_{sza} from Meteosat-8 is approximately 35 degrees higher than that from Himawari-8, Heliosat-3 estimates based on Meteosat-8 images have 4 and 4.5 percentage points higher rel. RMSE compared to CAMS Himawari-8, even after applying the corrections. When compared to NSRDB Himawari-8, the Heliosat-3 estimated GHI from Meteosat-8 images have 1.1 and 1.6 percentage points higher rel. RMSE at Central Highlands and Tri An, respectively.

3.2. Influence of season on error reduction

Figs. 7–11 present the monthly rel. RMSE of the Heliosat-3 estimated GHI at 15 min resolution for the uncorrected, parallax corrected and parallax and cloud shadow corrected cases at the five sites during the analysis year 2018. At the Gurgaon, Tiruvallur and Feni sites – located relatively close to the SSP of Meteosat-8 and within 61° θ_{sza} (see Table 1) – the rel. RMSE values are comparable. However, there is a significant increase in rel. RMSE at the Feni site during the cloudy summer monsoon months (June to September) and the preceding Nor'wester

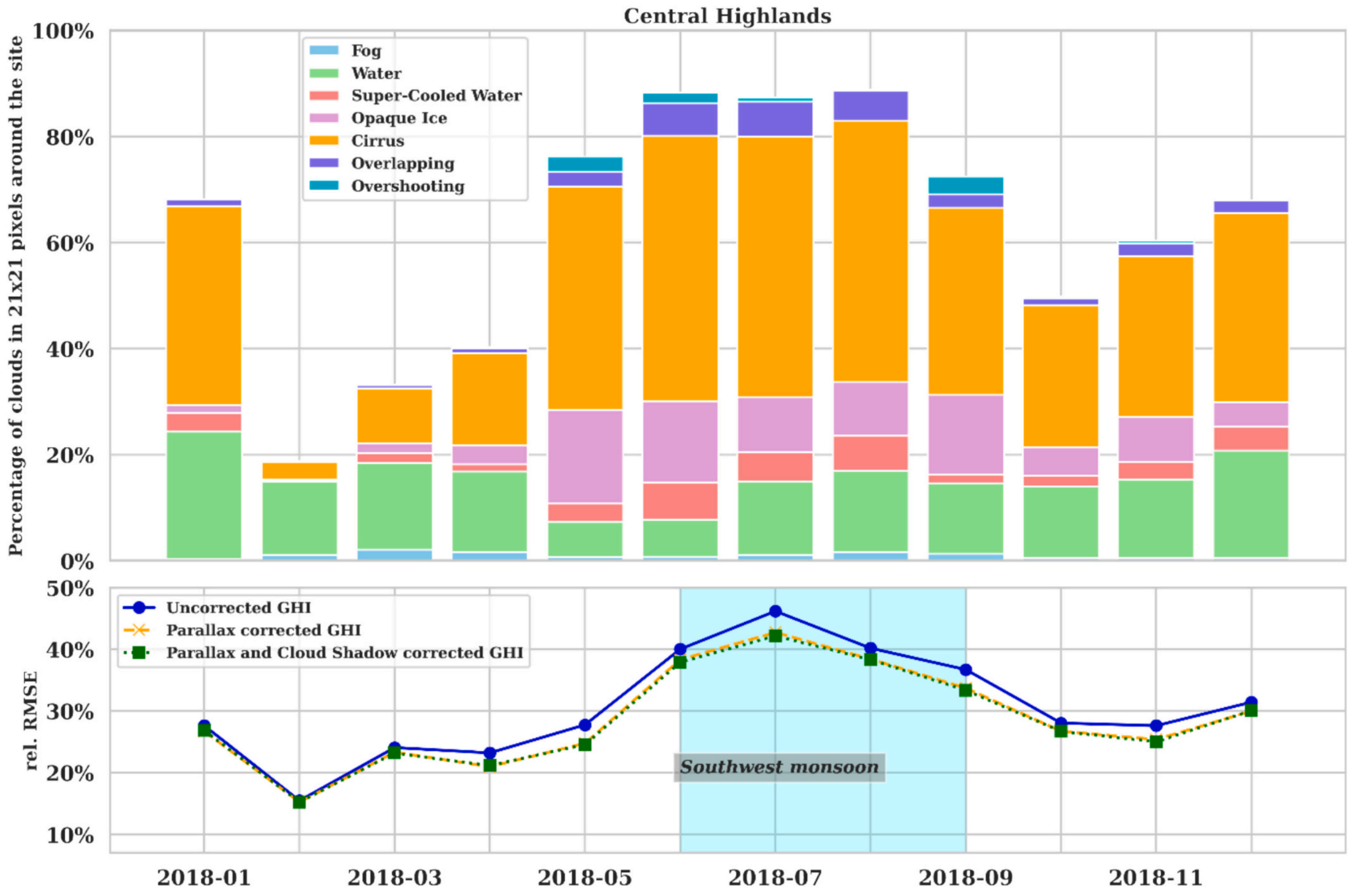

Fig. 10. (a) Percentage of cloudy pixels according to CLAVR-X cloud type retrieved from 21 × 21 pixels of Himawari-8 image around the site (b) monthly rel. RMSE in 15 min resolution Heliosat-3 estimated GHI at the Central Highlands site.

period (April to May) (see Fig. 9). Central Highlands and Tri An show consistently high rel. RMSE throughout the year due to their large θ_{sza} values from Meteosat-8. The reference cloud BRF (ρ_c) used in the Heliosat-3 method is optimized for smaller θ_{sza} [78], and when combined with the reduced pixel spatial resolution at higher θ_{sza} values, this contributes to the high rel. RMSE observed at Central Highlands and Tri An.

It is evident that applying the parallax correction to the CI image alone does not significantly improve the final estimated GHI. In some cases, it may even increase the error in the satellite-estimated GHI. This increase is observed during four months at Gurgaon, four months at Tiruvallur, three months at Feni and two months at Tri An. At Central Highlands, which has the highest θ_{sza} from Meteosat-8, parallax correction alone does not result in an increase in error during any month (see Fig. 10). The greatest improvement in average monthly rel. RMSE from parallax correction alone occurs at Gurgaon in April (from 11.1 % to 10.5 %), at Tiruvallur in May (from 17.2 % to 16.4 %), at Feni in May (from 37.3 % to 31.2 %), at Central Highlands in July (from 46.2 % to 42.7 %) and at Tri An in December (from 25.9 % to 21.5 %).

Applying the parallax correction followed by cloud shadow projection results in a noticeable improvement in the final estimated GHI at all the sites. It does not lead to an increase in the monthly rel. RMSE at any of the sites. The highest improvement in average monthly rel. RMSE of the final corrected GHI is observed at Gurgaon in August (from 25.1 % to 21.7 %), at Tiruvallur in July (from 14.5 % to 11.8 %), at Feni in May (from 37.3 % to 28.8 %), at Central Highlands in July (from 46.2 % to 42.2 %) and at Tri An in December (from 25.9 % to 20.8 %).

At all the sites, the error in Heliosat-3 estimated GHI increases with the increase in frequency of opaque ice, cirrus, overshooting and overlapping clouds around the sites. The largest reductions in monthly rel. RMSE after applying the corrections are also observed during periods with these cloud types. This trend is mirrored in the absolute error of the satellite-estimated GHI every 15 min (see Figs. A.1–A.5), where the error, as well as the improvement due to the corrections, is greater in the presence of these particular cloud types.

Sossan [45] reduced the errors in satellite-estimated GHI due to spatial resolution and parallax effect by statistical de-biasing. The authors suggested that real-time correction may be challenging without highly resolved data. In our study, we used pixel-wise CTH information interpolated to the spatial resolution of the 0.6 μm visible channel image to geolocate clouds and their shadows. This resulted in a reduction in the monthly rel. RMSE at all sites for each of the 12 months in 2018. However, applying the parallax shift alone led to an increase in rel. RMSE during multiple months at all sites. Interestingly, sites with higher values of θ_{sza} from Meteosat-8, such as Feni, Central Highlands, and Tri An, experienced fewer months where rel. RMSE increased due to parallax correction alone. Beyer et al. [55] showed that the RMSE of the linear regression between the satellite-estimated CI and ground-measured k_c decreased from 0.156 to 0.145 after the correction, based on two months of data from ground stations distributed over a relatively small area of approximately 700 km × 500 km. However, this average improvement does not provide insights into the performance of the correction across different seasons or under varying cloud types and cloud vertical extents. In contrast, our results show that applying both parallax and cloud shadow shifts, using bilinear interpolation, leads to the largest reductions in rel. RMSE during periods when opaque ice, cirrus, overshooting and overlapping clouds occur more frequently. Cirrus and overshooting clouds, in particular, contribute to the greatest

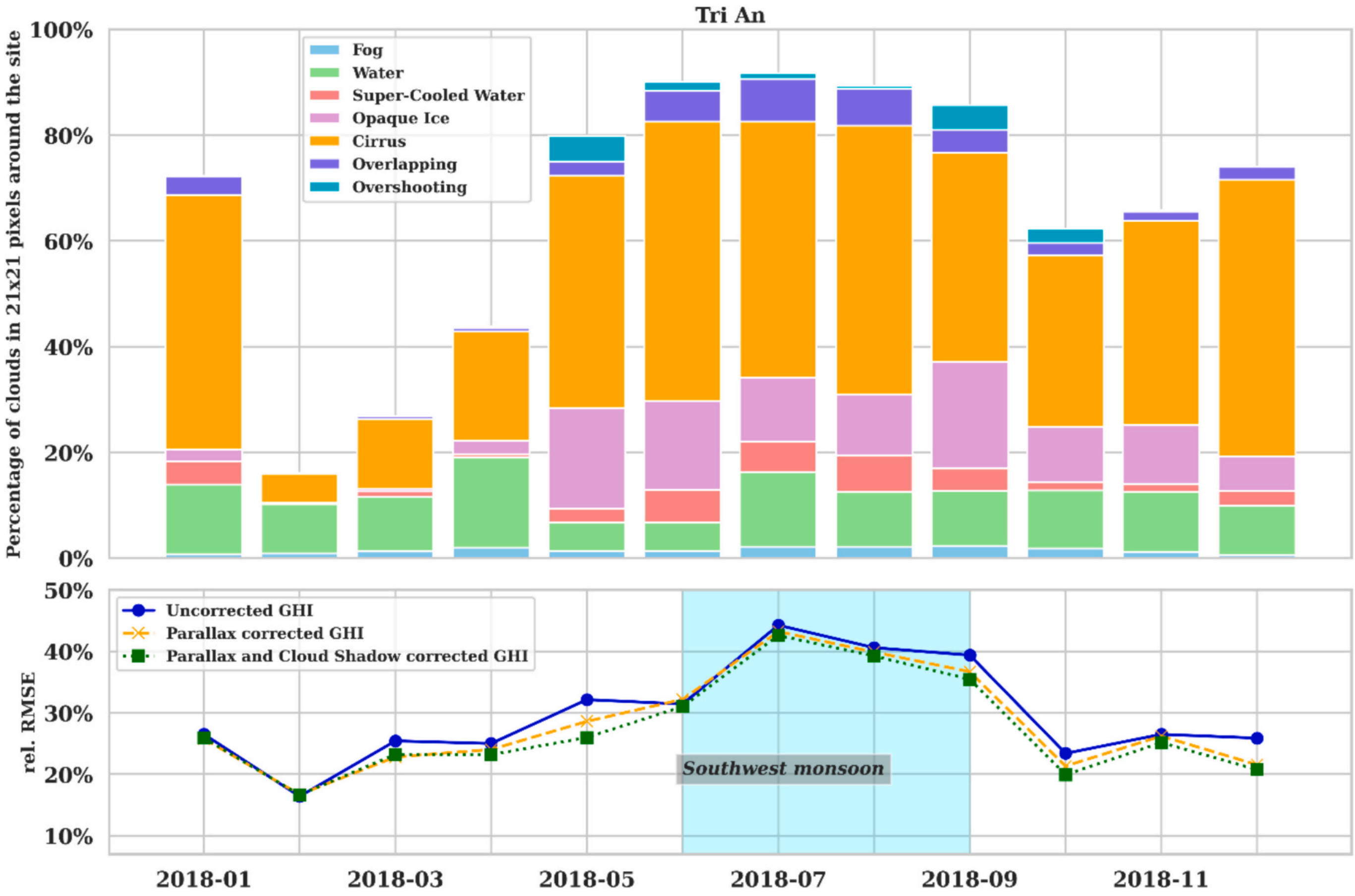

Fig. 11. (a) Percentage of cloudy pixels according to CLAVR-X cloud type retrieved from 21 × 21 pixels of Himawari-8 image around the site (b) monthly rel. RMSE in 15 min resolution Heliosat-3 estimated GHI at the Tri An site.

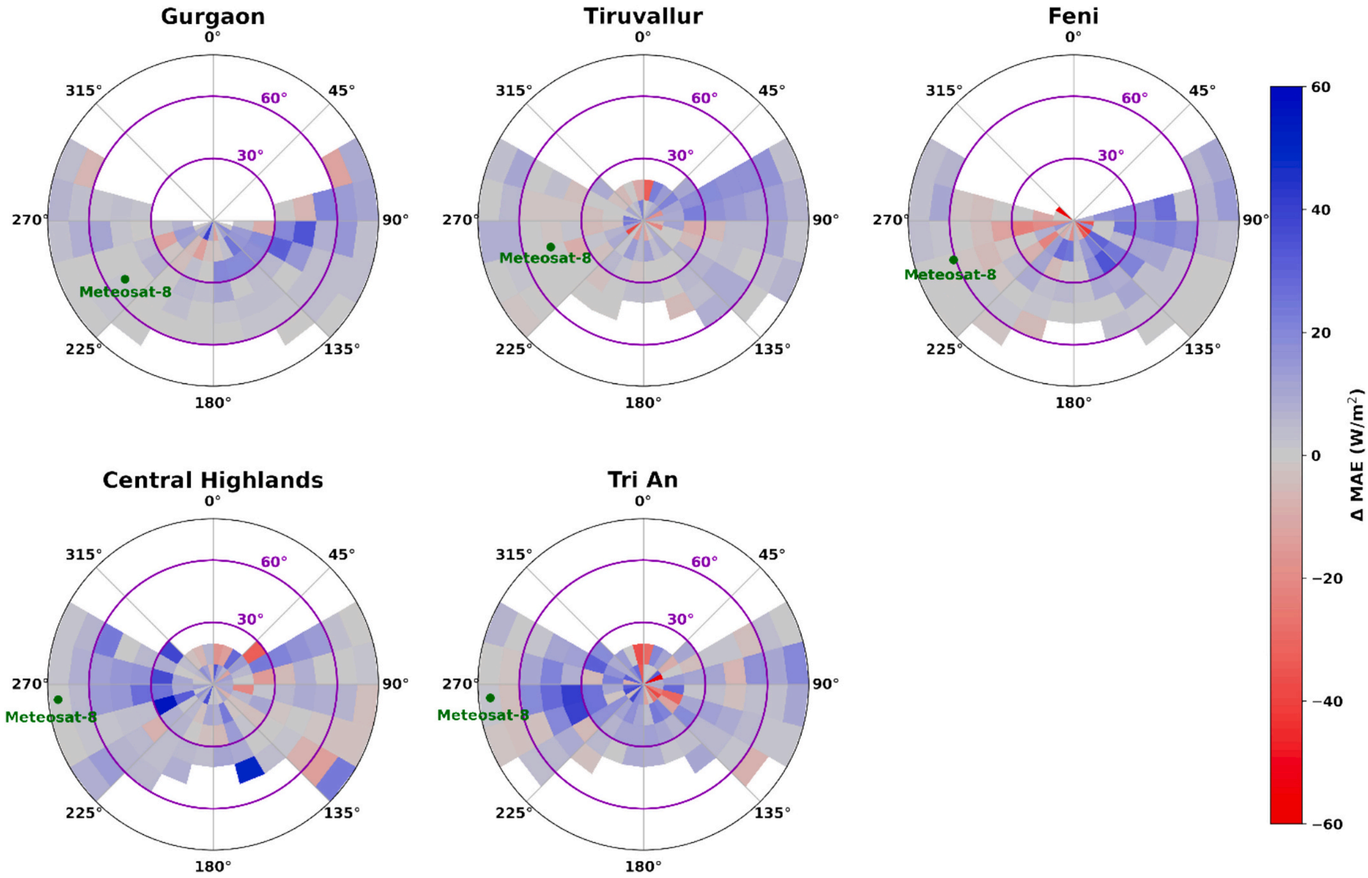

Fig. 12. Polar plot of the change in MAE for different solar zenith (θ_z) and azimuth angle (φ) bins, with $\theta_z < 80^\circ$, after applying the corrections. The locations of the Meteosat-8 satellite with respect to the sites are shown with a green point. (For interpretation of the references to colour in this figure legend, the reader is referred to the web version of this article.)

cloud shadow displacement from the actual cloud location due to their considerable heights. Overshooting clouds, which are associated with deep convective systems, typically exhibit substantial vertical extents. Opaque ice clouds have a much greater impact on the extinction of incoming GHI than water clouds [79]. Consequently, errors in satellite-estimated GHI are amplified when the shadows of these clouds are inaccurately represented. Additionally, modeling the effects of overlapping or multi-layered clouds on solar irradiance extinction is inherently complex [80]. These cloud types, which are predominantly observed during the convective monsoon period at all sites, lead to significant errors in GHI estimates. A significant reduction in rel. RMSE is also observed at Feni during the Nor'wester period from April to May. This is attributed to the frequent occurrence of overshooting, overlapping, cirrus, and opaque ice clouds, which are common during severe local convective storms, or Nor'westers, that prevail in the pre-southwest monsoon season in this region [23]. In fact, thunderstorms are more frequent in this region during April and May than during the peak monsoon months of July and August [24]. This may explain the larger reductions in rel. RMSE during the Nor'wester period compared to the summer monsoon period at Feni.

3.3. *Influence of sun-site-satellite orientation on error reduction*

Fig. 12 shows that the largest reductions in MAE of the 15 min resolution Heliosat-3 estimated GHI at Gurgaon, Tiruvallur and Feni occur when the co-scattering angle (ψ) – the angle between the azimuth of the sun and the satellite relative to the site – is large. Conversely, little to no reduction, or even an increase in MAE, is observed for small ψ values at these three sites. This is particularly observed for $\theta_z \geq 10^\circ$, while for lower θ_z values the distribution of reduction or increase tends to be random. Fig. 13 further illustrates that the reduction in monthly RMSE of the 15 min resolution Heliosat-3 estimated GHI is significantly greater in the pre-noon period (solar azimuth angle $\varphi < 180^\circ$) than in the post-noon period (solar azimuth angle $\varphi > 180^\circ$), after applying the parallax and cloud shadow corrections. This can be explained by the sun-site-satellite geometry at the three sites, as shown in Fig. 14. All three are relatively close to the SSP of Meteosat-8 and within 61° θ_{sza}. Corrections during the pre-noon period have the largest impact, as ψ is higher during this period, resulting in a greater separation between the apparent cloud location and the actual cloud shadow. In contrast, this separation decreases in the post-noon period, where ψ values are lower. Performing parallax correction alone often increases the monthly RMSE in the post-noon period, while a reduction is typically seen during pre-noon. This

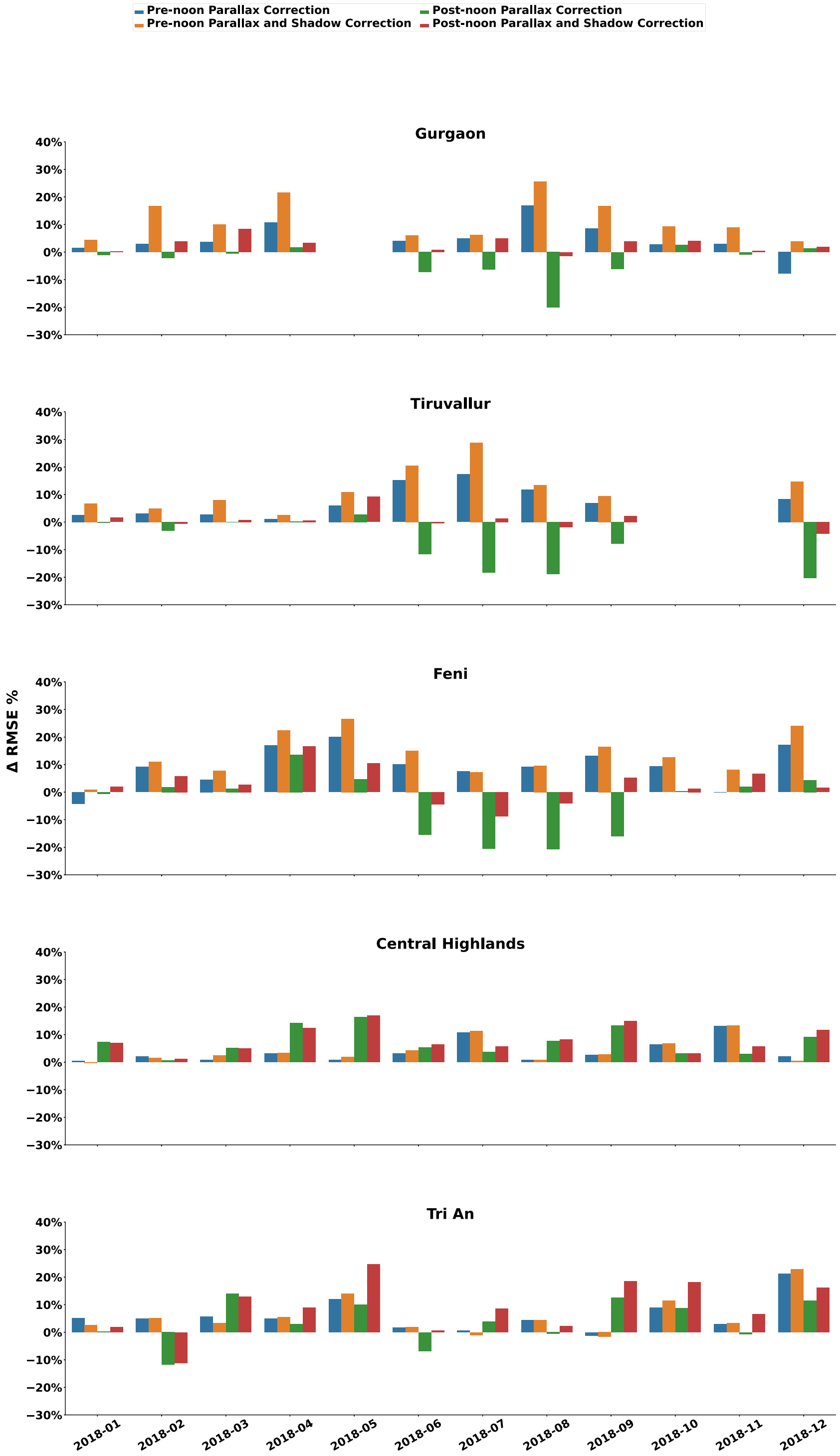

Fig. 13. Monthly RMSE reduction in satellite estimated 15 min resolution GHI during pre-noon and post-noon time at (a) Gurgaon, (b) Tiruvallur, (c) Feni, (d) Central Highlands and (e) Tri An.

effect is particularly pronounced during the southwest monsoon season (June–September) for Gurgaon, Tiruvallur and Feni. At the Tiruvallur site, a similarly large increase in monthly RMSE is observed in the post-noon period of the northeast monsoon season (October–December). Even applying the cloud shadow displacement step does not significantly reduce the RMSE during the post-noon period of the monsoon months at these sites.

The greatest reduction in the MAE of 15 min resolution Heliosat-3 estimated GHI at Central Highlands and Tri An occurs for low ψ values (see Fig. 12). These two sites, located near the eastern edge of the Meteosat-8 field of view (see Fig. 1) with θ_{sza} exceeding 70° (see Table 1), face limitations in cloud information to the east when the sun is in the eastern half of the horizon during the pre-noon period. As a result, the potential for reducing the monthly RMSE in GHI by applying the parallax and cloud shadow corrections during pre-noon is significantly less than indicated in Fig. 14. Most cloud information in the Meteosat-8 field of view is available from pixels west of the sites, providing sufficient cloud information during the post-noon period to apply the

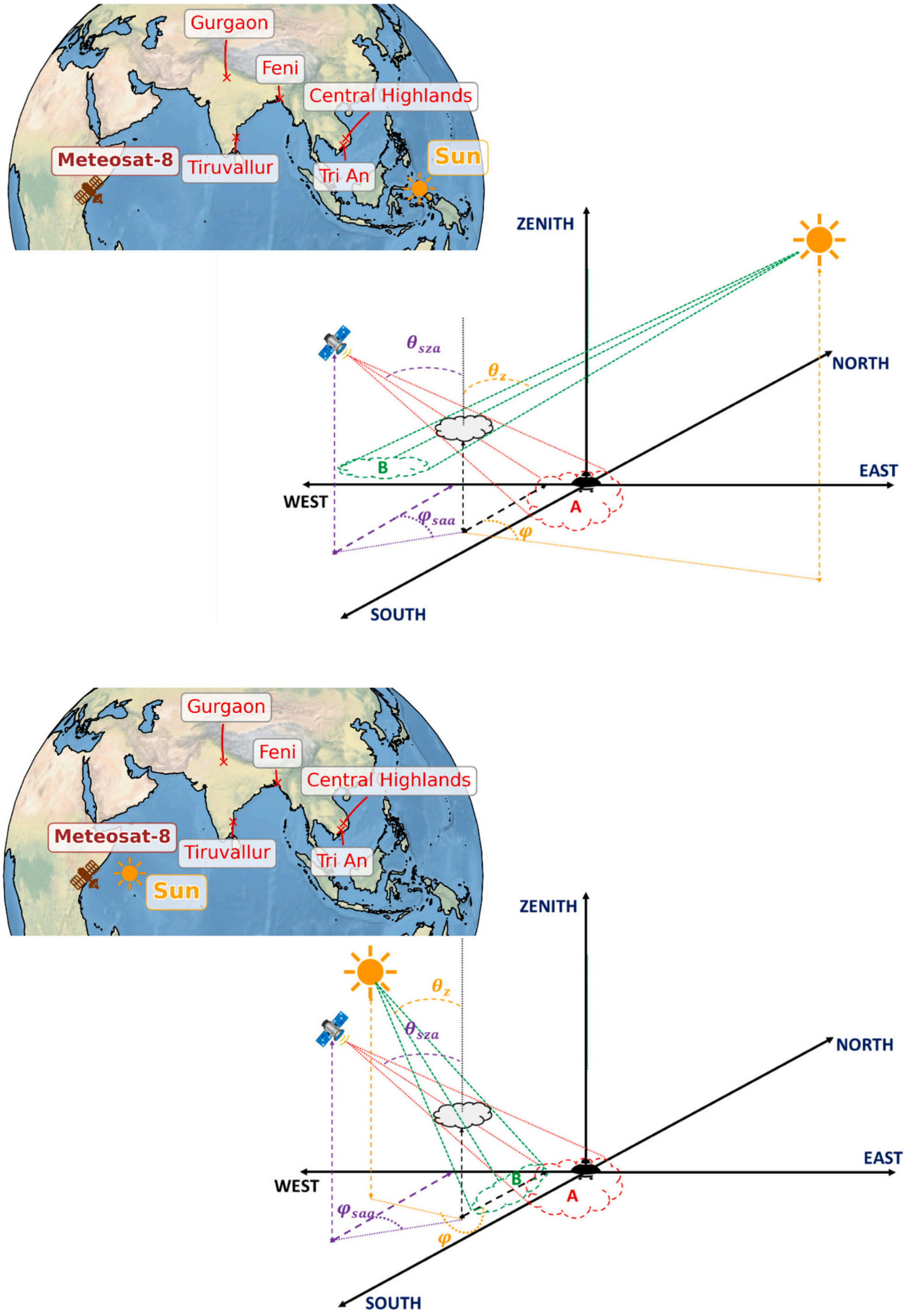

Fig. 14. The relative position of the satellite and the sun with respect to the sites during (a) the pre-noon period $\varphi < 180^{\circ}$ shown on the top and (b) the post-noon period $\varphi \geq 180^{\circ}$ shown in the bottom (apparent cloud location A, marked in red and the actual cloud shadow location B, marked in green). (For interpretation of the references to colour in this figure legend, the reader is referred to the web version of this article.)

corrections effectively. Additionally, the large θ_{sza} increases the potential for reducing monthly RMSE via parallax correction alone. Therefore, at these two sites, a greater reduction in RMSE is observed in the post-noon period.

From Fig. 14, it can also be observed that the Tiruvallur, Central Highlands and Tri An sites have valid GHI datapoints and finite reduction or increase in MAE for $\varphi \in [315^{\circ}, 45^{\circ}]$ and $\theta_z < 20^{\circ}$. This phenomenon occurs because these sites, located within 15° N of the equator, experience the sun to the north during mid-day in the summer months. Consequently, this unique positioning affects the observed GHI data.

3.4. *Influence of CTH on error reduction*

As shown in Fig. 15, the corrections have no impact on the median value of MAPE below a CTH of 2 km at any site. This aligns with the findings of Miller et al. [56], who simulated the displacement of the shadow from the apparent cloud location for various CTH and θ_z values. They observed that for low CTH values, shadow displacement is negligible, except at very high θ_z during morning and evening. At Gurgaon

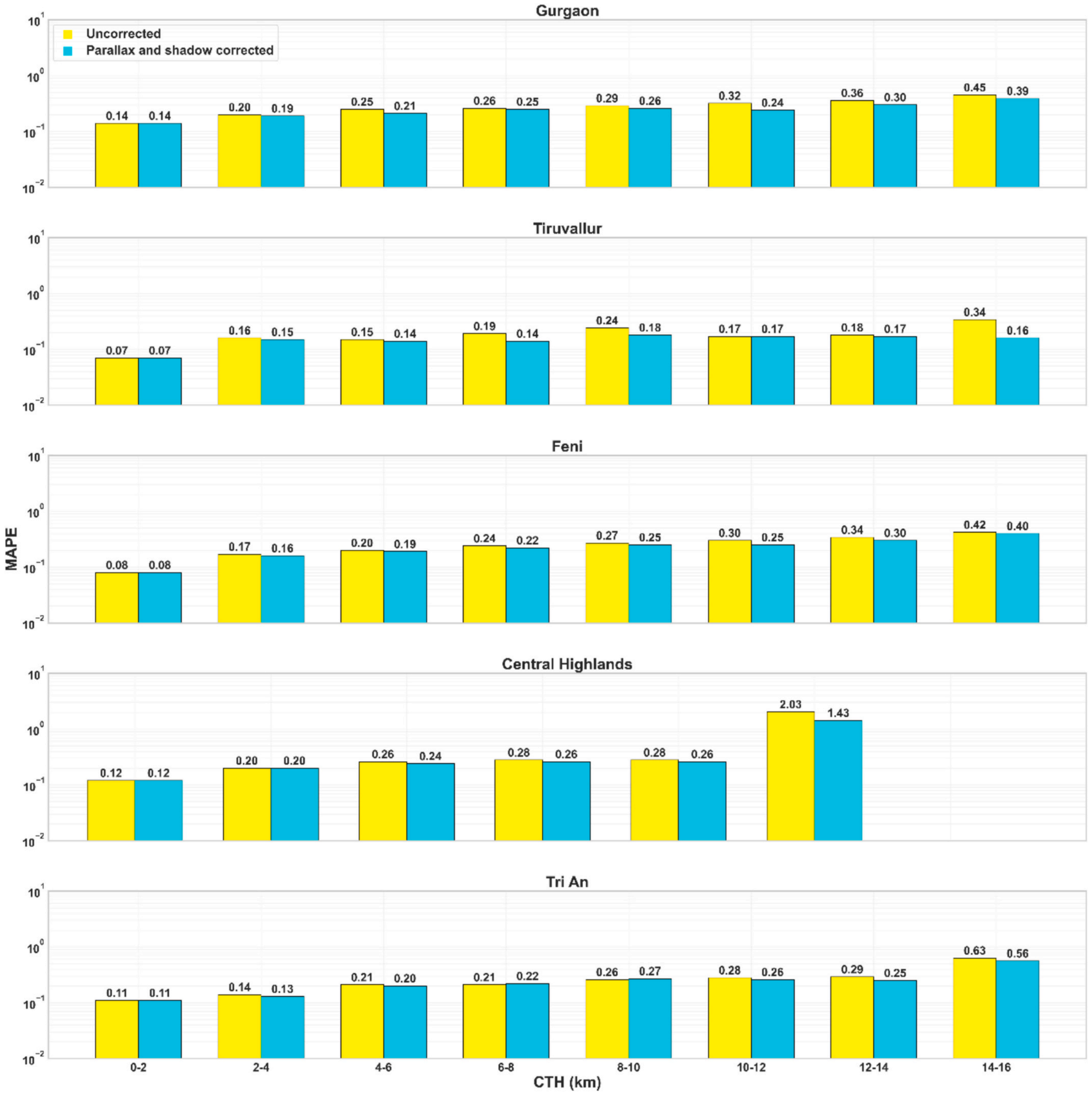

Fig. 15. Mean Absolute Percentage Error in terms of fraction for different cloud top height (CTH) bins at (a) Gurgaon, (b) Tiruvallur, (c) Feni, (d) Central Highlands and (e) Tri An.

and Tiruvallur, which are the closest to the SSP of Meteosat-8, a noticeable reduction in MAPE (by 4–6 percentage points) is observed for CTH values between 4 and 10 km after applying the corrections. In contrast, significant reductions at Feni, Central Highlands and Tri An only occur when the CTH exceeds 10 km. This can be explained by the fact that the nominal 3 km × 3 km spatial resolution of Meteosat-8's visible or infrared channel images is achieved only at the SSP, and the pixel resolution degrades with increasing θ_{sza}. This observation is consistent with the explanation provided by Wu et al. [44], who noted that parallax effects are relatively small when CTH is low relative to the horizontal resolution of the satellite image pixel. The largest MAPE in uncorrected Heliosat-3 estimated GHI occur when CTH exceeds 10 km at each site, due to (i) the large displacement of cloud shadows from their apparent pixel locations at high CTH values and (ii) the presence of multi-layered cloud distributions, which often accompany large CTHs during certain weather conditions [81] and are not modeled in Heliosat-3. The greatest reduction in the median value of MAPE after applying corrections also occurs at high CTH values across all sites. However, the corrections do not account for multi-layered cloud distributions, and due to the coarser resolution of the original CTH dataset (9 km × 9 km at the SSP), misassignments of CTH values to cloudy pixels can lead to errors in cloud shadow displacement. These errors increase with CTH, resulting in relatively high MAPE values even after the corrections are applied.

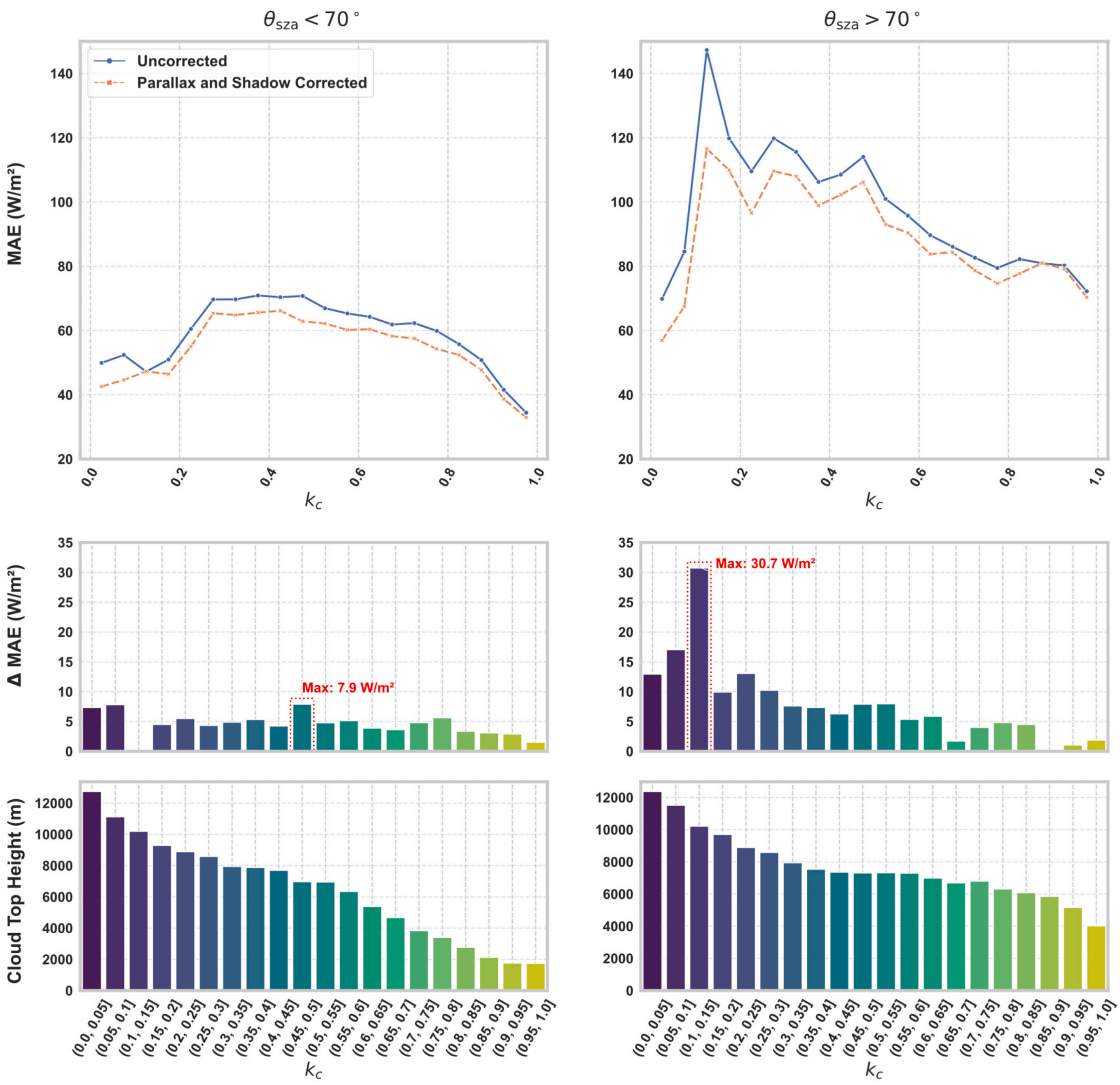

Fig. 16. Variation in MAE, reduction in MAE and average CTH as a function of k_c at (a) Gurgaon, Tiruvallur and Feni (shown on the left) and (b) Central Highlands and Tri An (shown on the right).

3.5. Influence of cloudiness on error and reduction

As shown in Fig. 16a, the binned MAE is highest during partly cloudy conditions, characterized by intermediate k_c values, for both the uncorrected and corrected Heliosat-3 GHI estimates at 15 min resolution across all the sites. This aligns with the findings of Marie-Joseph et al. [43], who observed a bell-shaped curve for the bias in GHI against the ground-derived clearness index k_t, with the maximum bias occurring under partly cloudy skies. They attributed this to the parallax effect, noting that it is most significant when cloud cover is fragmented and spatially variable. In contrast, the effect is less pronounced when cloud cover is homogeneous or the sky is clear, as shifting uniform cloud conditions has little impact. This partly explains the bell-shaped curve observed in their study. Sossan [45] similarly reported the largest discrepancies between satellite-derived and ground-based pyranometer measurements during partly cloudy conditions.

At Gurgaon, Tiruvallur, and Feni, the largest reduction in MAE after applying parallax and cloud shadow corrections occurs in partly cloudy conditions (see Fig. 16a). However, significant reductions are also seen during overcast conditions with low k_c values. For Central Highlands and Tri An, located at the eastern edge of the Meteosat-8 field of view, notable reductions in the MAE of Heliosat-3 GHI estimates are also observed during partly cloudy conditions. However, the largest reductions occur in overcast situations, as shown in Fig. 16b. This is likely due to the actual spatial resolution at these sites being lower than the nominal 3 km × 3 km resolution at the SSP, making it difficult to resolve fragmented clouds in any case. In contrast, overcast conditions tend to feature more extensive, continuous cloud coverage, often with higher CTH. Higher CTH combined with large θ_{sza} leads to larger parallax and cloud shadow displacements, explaining the greater potential for error correction in these scenarios. Consequently, applying parallax and cloud shadow corrections yields the greatest benefit during overcast conditions at these two sites.

3.6. Effect of the correction on satellite estimated GHI ramps

The ramp estimation error at 15 min resolution in both the corrected and the uncorrected satellite estimated GHI over the entire year 2018 at each of the five sites is shown in Table 4 for $\tau = 0.18$. τ value of 0.18 is large enough to obtain a ramp approximation error that is greater than the uncertainty of pyranometer measurement, as discussed in Vallance et al. [14]. After applying the corrections, the ramp score in $Wm^{-2}\,h^{-1}$ is reduced at all sites, indicating better alignment between the satellite-estimated and ground-measured GHI ramps (see Table 4). Comparatively larger ramp scores are observed at Feni, Central Highlands and Tri An, which are situated at higher θ_{sza} from the Meteosat-8 satellite.

Table 4
15-min ramp score in $Wm^{-2}\,h^{-1}$ of the satellite estimated GHI with respect to the ground measured GHI* for the year 2018, when τ is set to 0.18.

Site	Uncorrected Heliosat-3 GHI	Parallax and Shadow corrected Heliosat-3 GHI
Gurgaon	93	89
Tiruvallur	97	96
Feni	130	125
Central Highlands	218	214
Tri An	193	189

* Only the valid daytime datapoints mentioned in Table 1.

To examine the sensitivity of ramp score improvement relative to τ values, a practically applicable range of τ must be chosen. The average 15-min ramp in ground measured GHI across all five sites is approximately 0.06 times the daily maximum of $GHI_{clearsky}$. This value closely aligns with the minimum τ value of 0.08 chosen in Vallance et al. [14], which ensures reliable ramp detection given the inherent uncertainty in GHI measurements taken with pyranometers. Since this analysis focuses on the improvement in cloud-induced ramp detection after applying the corrections, the upper τ limit must ensure that the percentage of points detected as ramps in satellite-estimated GHI remains higher than those

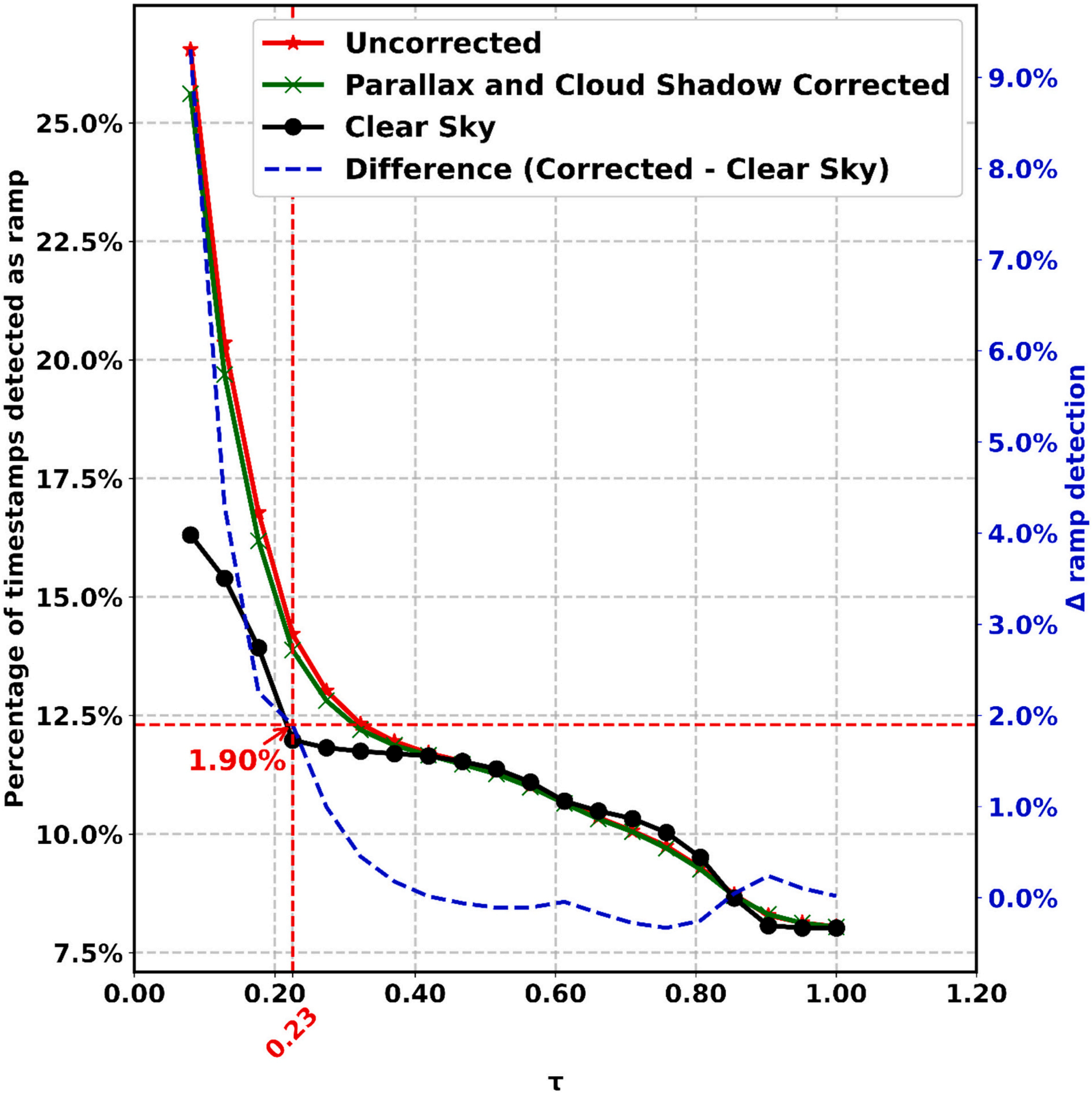

Fig. 17. Change in ramp detection capability for varying τ values.

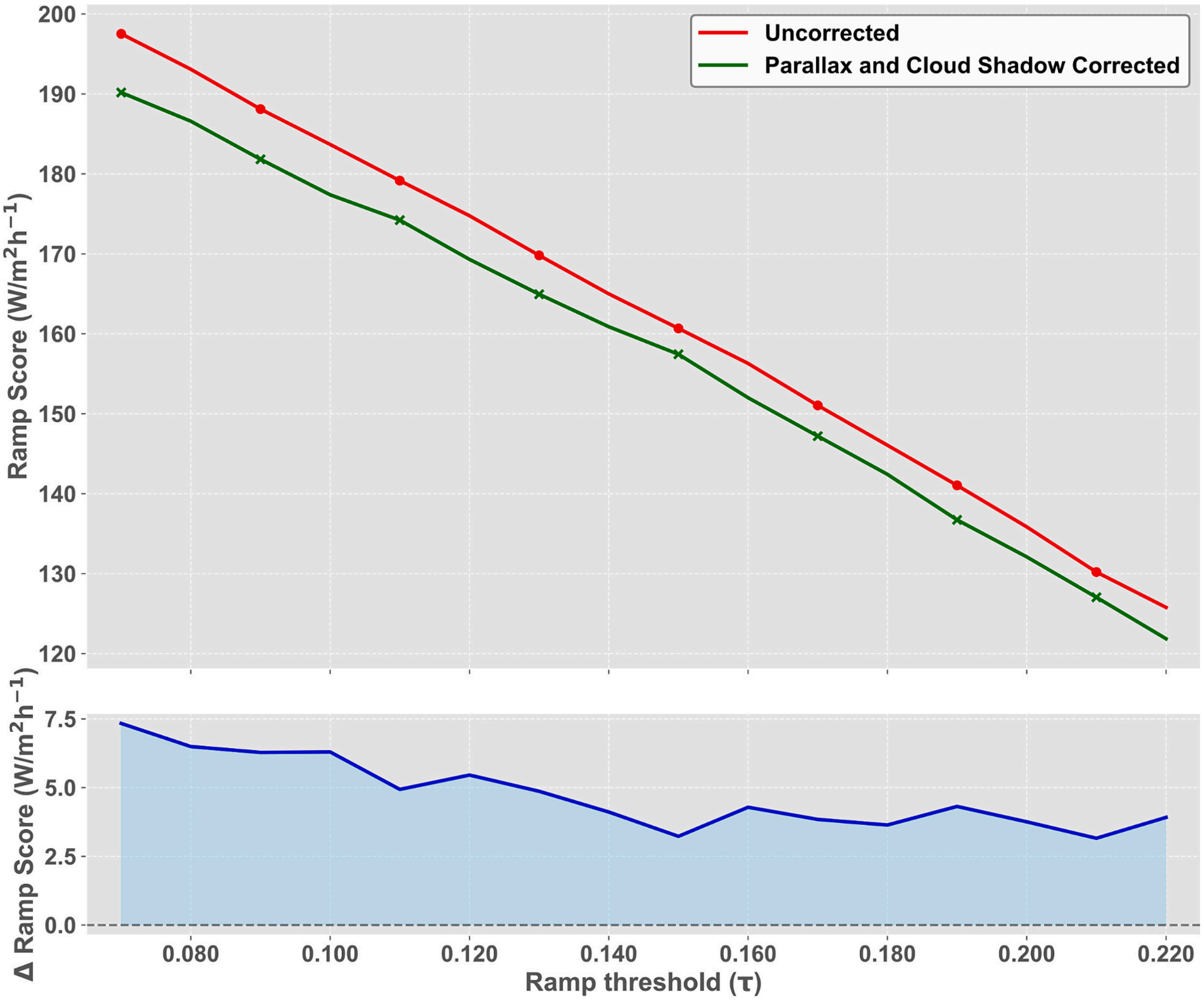

Fig. 18. Variation of the ramp score averaged across all sites with $\tau \in (0.07, 0.22)$.

detected solely due to the diurnal variation of $GHI_{clearsky}$. As shown in Fig. 17, when τ reaches 0.23, the difference in timestamps classified as ramps between satellite-estimated GHI and clear-sky GHI falls to 1.90 percentage points. This margin of 2 % point difference is considered practical, as ramp thresholds should remain low enough to distinguish cloud-induced fluctuations from the inherent diurnal variation in $GHI_{clearsky}$. Testing the sensitivity of the improvement in ramp score for $\tau \in [0.07, 0.22])$ allows meaningful analysis of cloud-induced fluctuations, within the context of this work.

Due to the lower spatial resolution of the satellite image pixels compared to the point measurements from pyranometers, satellite-estimated GHI cannot capture the same degree of variability as ground-measured GHI, particularly at a 15 min temporal resolution. Consequently, at lower τ values, even small-scale fluctuations in ground-measured data are detected as ramps across all sites, leading to higher ramp scores for both corrected and uncorrected Heliosat-3 GHI estimates. As τ increases, much of this variability is masked due to the higher tolerance for fluctuations in the SDA algorithm, leading to improved ramp scores in both Heliosat-3 datasets. Nevertheless, the corrected GHI estimates consistently show lower ramp scores than the uncorrected estimates across the entire range of τ values considered in the sensitivity analysis, as shown in Fig. 18. This trend is also observed at all the individual sites (see Figs. B.1–B.5).

Fig. 19 provides two detailed examples to illustrate the ability of satellite-estimated GHI to capture actual GHI ramps measured at the ground surface. On July 31, 2018, at Gurgaon, applying the corrections improved the overall ramp score from 68 $\text{Wm}^{-2}\ \text{h}^{-1}$ to 50 $\text{Wm}^{-2}\ \text{h}^{-1}$. While the ramp score improved by 24 $\text{Wm}^{-2}\ \text{h}^{-1}$ during the pre-noon period, only a smaller improvement of 13 $\text{Wm}^{-2}\ \text{h}^{-1}$ was observed during the post-noon period (see Fig. 19b). Fig. 19a shows another case where applying the corrections led to an increase in the overall ramp score from 76 $\text{Wm}^{-2}\ \text{h}^{-1}$ to 84 $\text{Wm}^{-2}\ \text{h}^{-1}$ on February 5, 2018, at Gurgaon, due to deteriorating GHI ramp estimation in the post-noon period. These limited improvements—or even deteriorations—in the post-noon period can be attributed to the effect of the sun-site-satellite orientation, as discussed in Section 3.3.

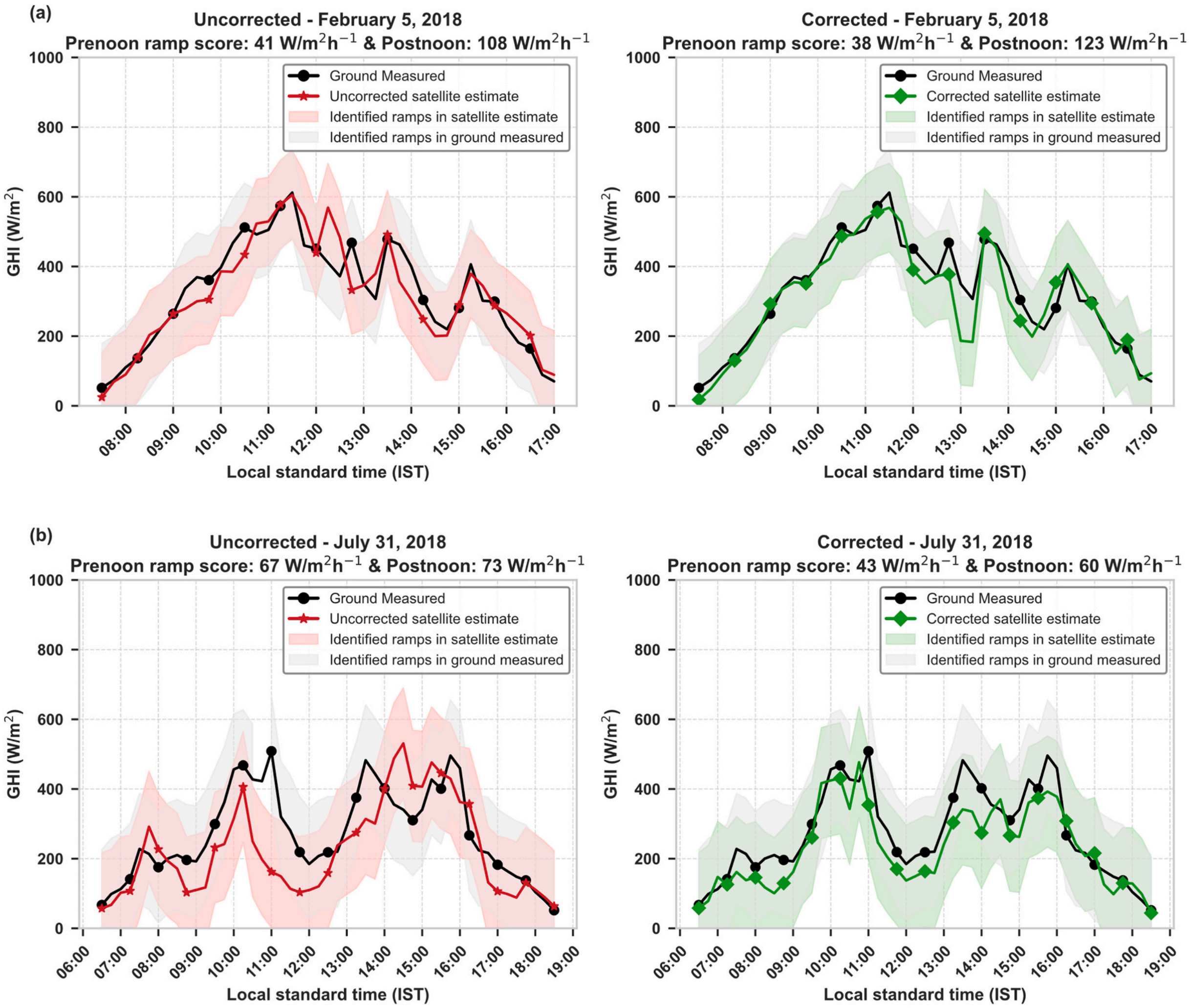

Note: Shaded regions represent identified ramp events based on threshold criteria

Fig. 19. Change in ramp score due to the parallax and cloud shadow correction (a) on 05.02.2018 and (b) 31.07.2018 at Gurgaon.

4. Conclusion

In this study, we presented a method that applies the parallax and cloud shadow shifts estimated with a gridded CTH dataset on Helioat-3 derived CI images from Meteosat-8 using bilinear interpolation to allow for sub-pixel displacement. By validating against one year of 15 min resolution ground-measured GHI data from five stations in South and Southeast Asia at varying viewing angles from the satellite, it has been shown that the rel. RMSE in the GHI estimated from the corrected CI images reduced from 23.8 % to 22.1 % over all the stations and the R^2 between the satellite-estimated and ground-measured GHI improved at each site. The reduction in rel. RMSE is found to be monotonically increasing with the decrease in the viewing zenith angle (θ_{sza}) of the site from the satellite. Similarly, the R^2 values also decrease with the increase in θ_{sza} of the site.

Benchmarking against the satellite estimated GHI datasets from NSRDB and CAMS radiation service showed that for the sites with a similar θ_{sza} in the three datasets, the Heliosat-3 estimated GHI from the corrected CI images at 15 min resolution outperformed NSRDB and CAMS estimated GHI by 4–7 percentage points and 2.5 percentage points of rel. RMSE respectively. For the two sites with 30° less θ_{sza} in the NSRDB and CAMS estimated GHI datasets, they showed 4–5 percentage points and 1–2 percentage points less rel. RMSE than the Heliosat-3 estimated GHI with corrections applied.

Seasonality in the monthly rel. RMSE of the 15 min resolution Heliosat-3 estimated GHI was observed at all sites, with larger errors coinciding with periods where opaque ice, cirrus, overlapping and overshooting clouds frequently occur. The occurrences of these cloud types increase during periods with intense atmospheric convection, such as the monsoon and the nor'wester seasons. Cirrus and overshooting clouds cause the highest displacement of the actual cloud shadow from the apparent cloud location due to their large height, contributing to significant errors in GHI estimates. The higher extinction caused by opaque ice clouds compared to water clouds further amplifies inaccuracies when their shadows are misrepresented. Additionally, the complexity of modeling the effects of overlapping clouds introduces further errors. Therefore, correcting the CI images during the monsoon and nor'wester periods, when these cloud types are most prevalent, resulted in the greatest reductions in relative RMSE.

The potential for reducing MAE by applying the corrections increases with the increase in co-scattering angle (ψ) between the azimuth of the sun and the satellite from the site, as the separation between the actual shadow location and the apparent cloud location increases with ψ. The impact of this on the 15 min resolution Heliosat-3 estimated GHI was significant at the three sites within 61° θ_{sza} from the satellite. Conversely, applying the corrections in the post-noon period has less impact and even increases the RMSE during monsoon months with intense atmospheric convection and large cloud heights. The actual reduction in MAE achievable during periods with large values of ψ is also limited by the availability of sufficient pixels of cloud information along the azimuth to the sun from the site. As a result, the two sites close to the eastern edge of the satellite showed little reduction in MAE for large ψ values when the sun was located in the eastern horizon with respect to the two sites. However, due to the high θ_{sza} at these two sites, correcting the parallax shift of the available cloud pixels to the west of the sites is sufficient to cause a significant reduction in MAE for low ψ values in the post-noon period. Additionally, sites like Tiruvallur, Central Highlands, and Tri An lie within 15° N, where the sun can be observed to the north during mid-day in the summer. This unique phenomenon occurs only in the tropics and is not seen elsewhere in the northern hemisphere.

Comparing the reduction in MAPE of the 15 min resolution Heliosat-3 estimated GHI for different cloud height bins showed that applying the corrections make no difference below a CTH of 2 km, and the reductions are noticeable only when the CTH is comparable to or higher than the pixel horizontal resolution. The largest reduction in the median value of MAPE was observed for CTH values exceeding 10 km. However, the MAPE in GHI after applying the corrections is still high for large CTH values due to the coarser resolution of the gridded CTH dataset (9 km × 9 km at SSP) and the lack of information on multi-layered clouds.

With the increase in the θ_{sza} value of the sites from the satellite, the degree of cloudiness for which the largest reduction in the MAE of the 15 min resolution Heliosat-3 estimated GHI occurs shifts from partly cloudy to overcast situations, where clouds with higher CTH frequently occur. While a similar magnitude of reduction in MAE was also observed at the two sites close to the edge of the satellite field of view during partly cloudy conditions, even greater reductions were seen during overcast conditions, likely due to the larger parallax and cloud shadow displacements caused by larger cloud heights and continuous cloud cover. This can be attributed to a combination of larger parallax and cloud shadow displacements caused by higher cloud tops and continuous cloud cover, as well as the lower effective spatial resolution at these two sites, which makes it harder to resolve fragmented clouds. In contrast, overcast conditions provide more easily resolvable extensive cloud coverage, increasing the potential for accurate corrections.

The sites with higher θ_{sza} from the satellite show larger discrepancies between the satellite- estimated and ground-measured GHI ramps at 15 min resolution. For this analysis, we selected a range of τ values where the ramp detection threshold is large enough to filter out fluctuations smaller than the average 15-min ground-measured ramp, but still low enough to capture more fluctuations in the satellite-estimated GHI than in the clear-sky estimates. Reducing τ, and thereby lowering the ramp detection threshold $\Delta GHI_{thresh,T_i}$, increases the error in satellite-based ramp estimation, as satellite-derived GHI cannot capture all small-scale fluctuations. Conversely, increasing τ improves ramp estimation accuracy by allowing higher threshold $\Delta GHI_{thresh,T_i}$ which masks out the small variations. Nevertheless, after applying parallax and cloud shadow correction on the CI images with bilinear interpolation, the satellite-estimated GHI ramps exhibit better agreement with ground-measured GHI ramps.

The method implemented in this study requires only the satellite viewing angles, CTH of the cloudy pixels and the solar position, making it easily applicable to images from any other geostationary platforms such as Meteosat-9, Meteosat-12 or Himawari-9. Similarly, the method could be applied to the legacy data from retired geostationary satellites for the long-term climatological analysis of solar energy potential at prospective PV sites or for studying the impact of special weather events on satellite retrieved GHI. The errors resulting from the use of a standard atmospheric profile in unstable atmospheric situations could be overcome in future studies using profiles from numerical weather prediction data. A potential direction for future research is the use of machine learning models to infer nonlinear parallax and shadow displacement patterns directly from imagery. However, such approaches were not pursued in this study due to the lack of spatially dense ground-truth data, which limits the ability to train generalizable models across large tropical regions. This study focused on improvement in satellite based GHI estimation due to parallax and cloud shadow correction, as accurate GHI estimations are a critical foundation for developing reliable forecasting methods for solar PV power output. Reliable power output forecasts derived from satellite images enable power plant owners and power traders to bid more optimally in the intra-day energy exchange markets and reduce financial losses due to inaccurate forecasts. For the grid operators, this translates to fewer intra-day imbalances at grid node points. Demonstrating the effectiveness of the method in improving GHI estimation accuracy highlights its potential applicability in future forecast models.

The work was carried out with funding from Deutscher Akademischer Austauschdienst (DAAD, German Academic Exchange Service)[grant number 57440921].

CRediT authorship contribution statement

Arindam Roy: Writing – review & editing, Writing – original draft, Visualization, Validation, Software, Resources, Project administration, Methodology, Investigation, Funding acquisition, Formal analysis, Data curation, Conceptualization. **Annette Hammer:** Writing – review & editing, Visualization, Supervision. **Detlev Heinemann:** Writing – review & editing, Visualization, Supervision, Project administration, Methodology, Funding acquisition. **Marion Schroedter-Homscheidt:** Writing – review & editing, Visualization, Project administration. **Ontje Lünsdorf:** Software, Resources, Methodology, Data curation. **Jorge Lezaca:** Software, Resources.

Declaration of competing interest

The authors declare that they have no known competing financial interests or personal relationships that could have appeared to influence the work reported in this paper.

Appendix A. Time series of the absolute error in satellite estimated GHI and the frequency of the different CLAVR-X cloud types at all the individual sites

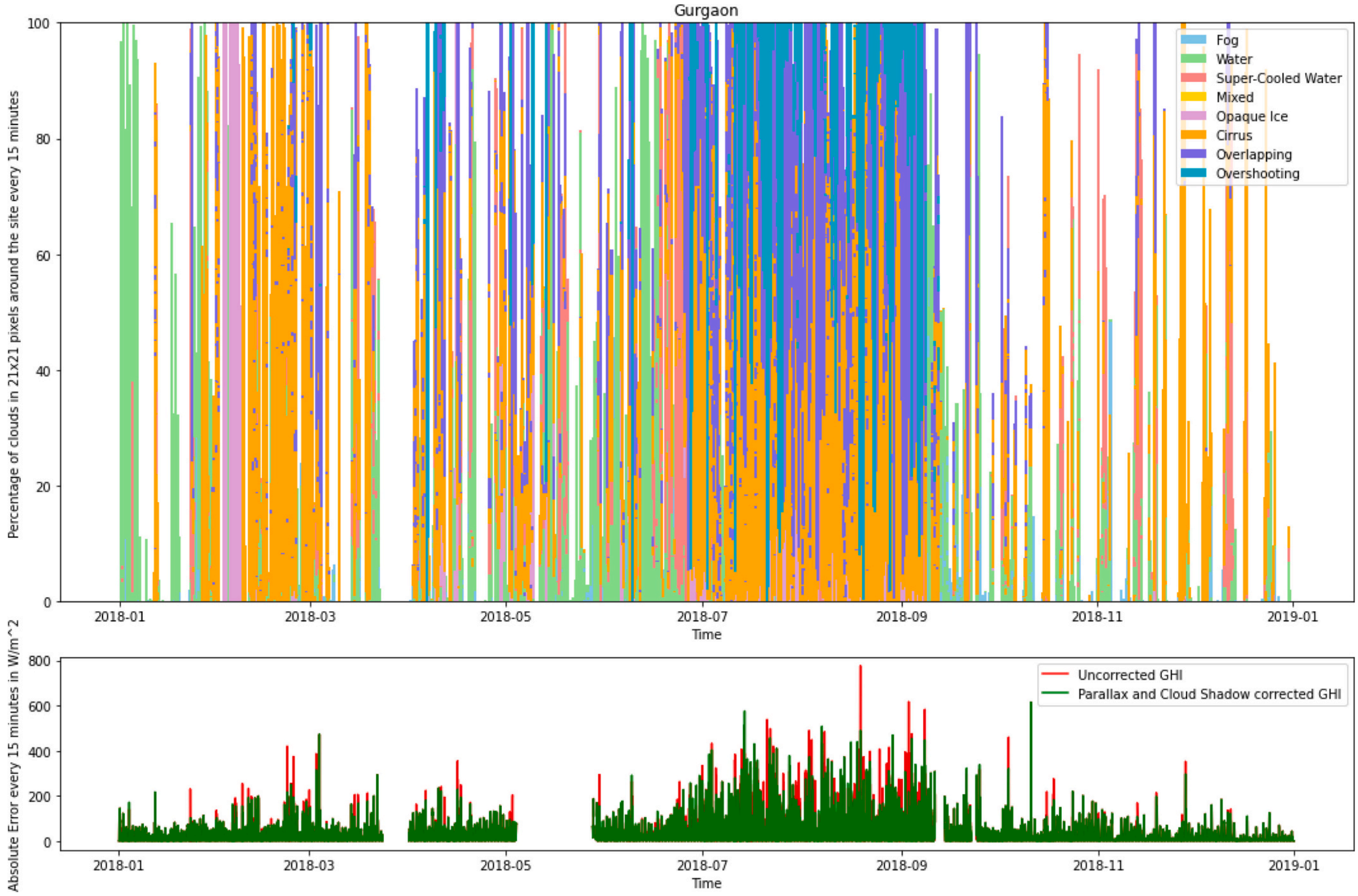

Fig. A.1. Gurgaon.

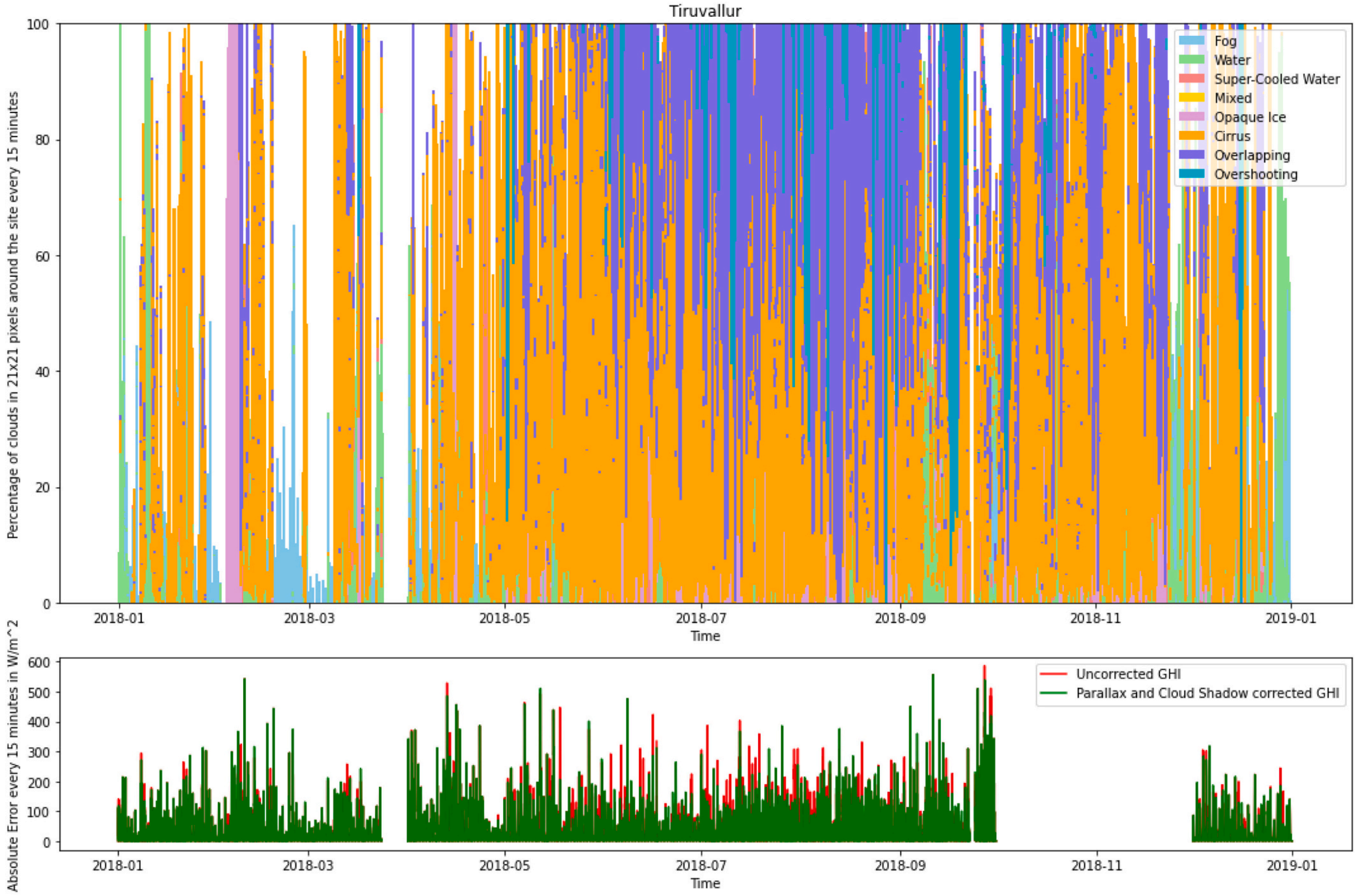

Fig. A.2. Tiruvallur.

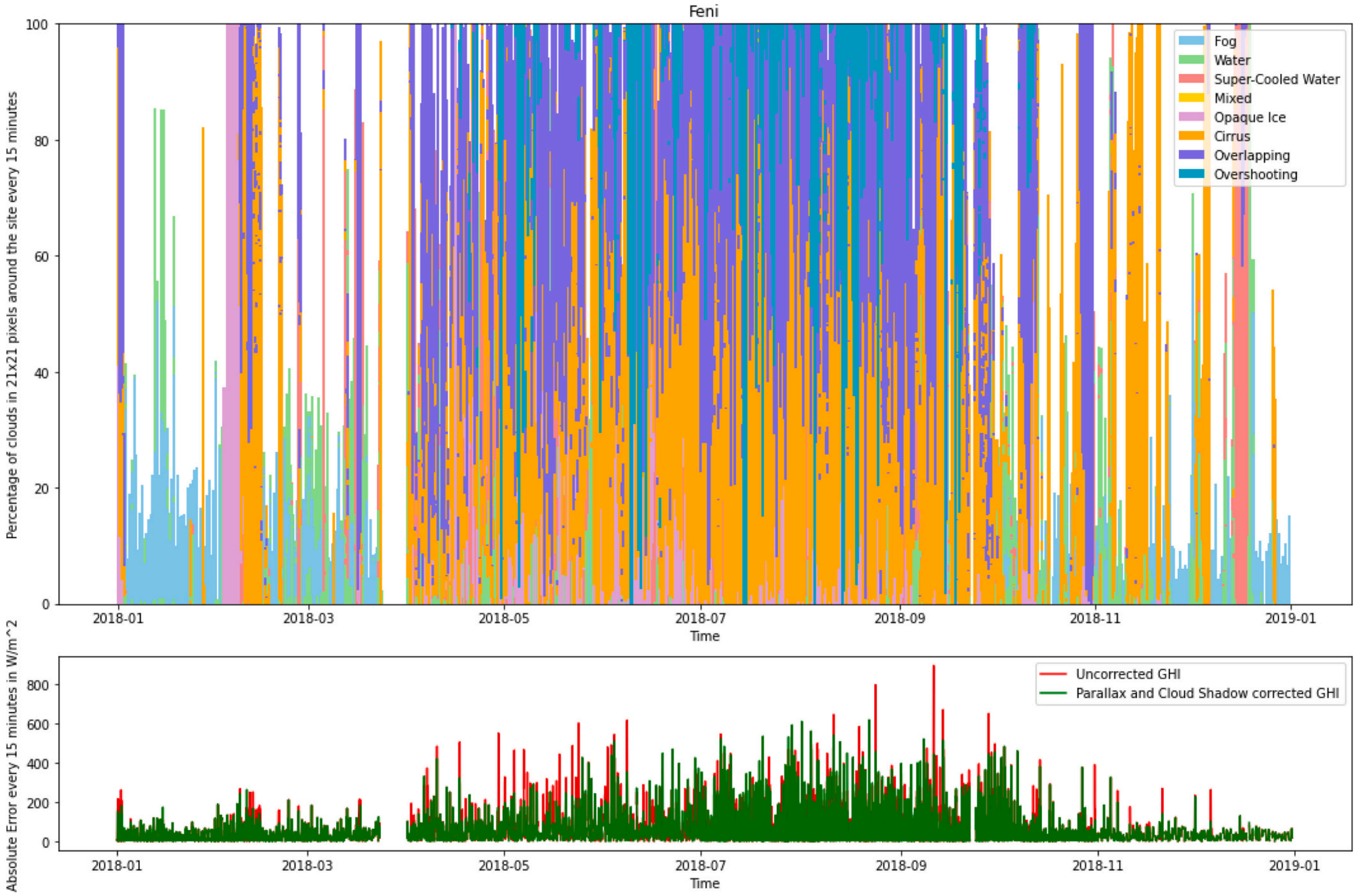
Feni
Percentage of clouds in 21x21 pixels around the site every 15 minutes
0
20
40
60
80
100
2018-01
2018-03
2018-05
2018-07
2018-09
2018-11
2019-01
Time
Fog
Water
Super-Cooled Water
Mixed
Opaque Ice
Cirrus
Overlapping
Overshooting
Absolute Error every 15 minutes in W/m^2
0
200
400
600
800
Uncorrected GHI
Parallax and Cloud Shadow corrected GHI

Fig. A.3. Feni.

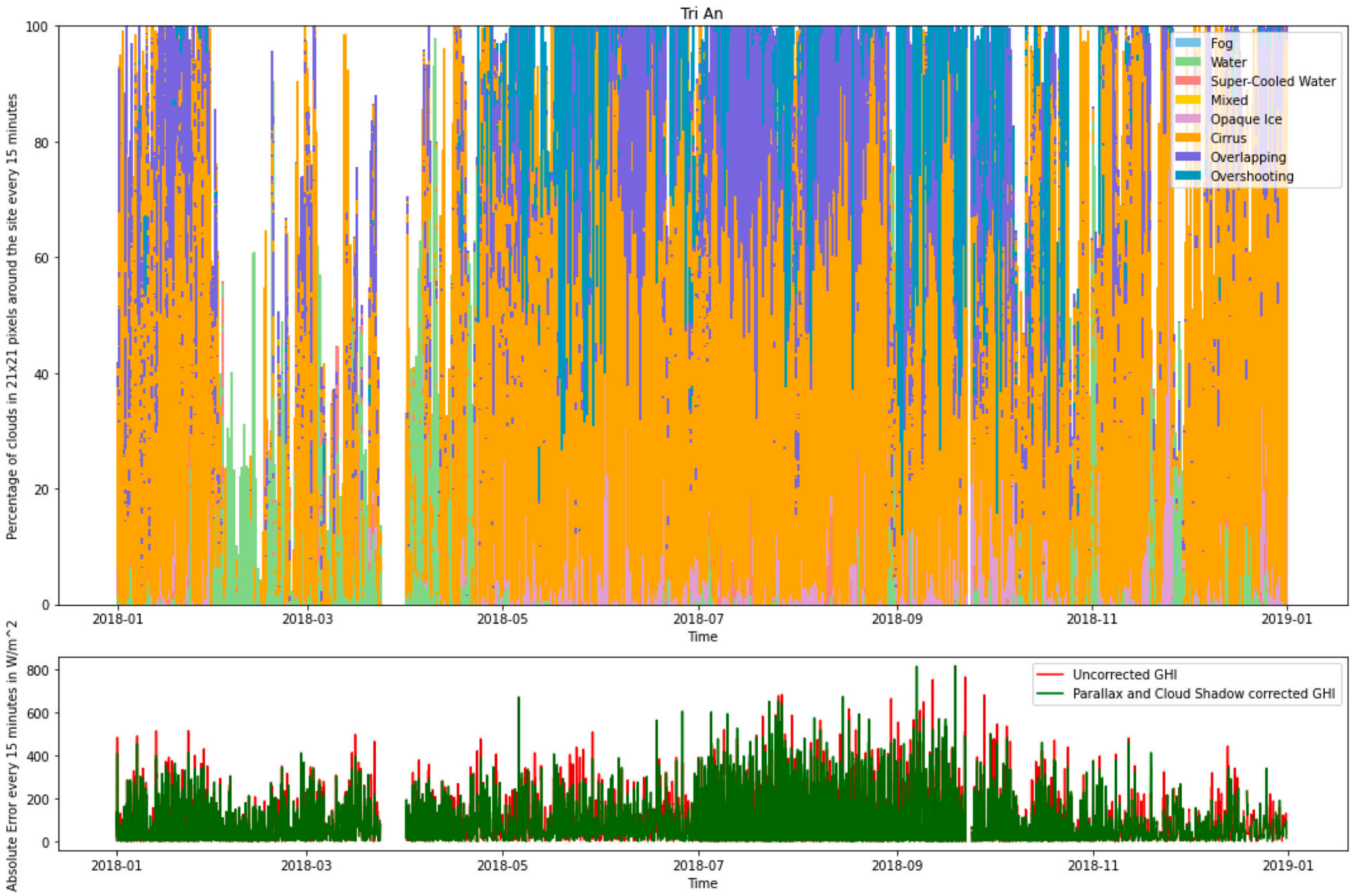
Tri An
100
80
60
40
20
0
Percentage of clouds in 21x21 pixels around the site every 15 minutes
Fog
Water
Super-Cooled Water
Mixed
Opaque Ice
Cirrus
Overlapping
Overshooting
2018-01
2018-03
2018-05
2018-07
2018-09
2018-11
2019-01
Time
800
600
400
200
0
Absolute Error every 15 minutes in W/m^2
Uncorrected GHI
Parallax and Cloud Shadow corrected GHI
2018-01
2018-03
2018-05
2018-07
2018-09
2018-11
2019-01
Time

Fig. A.4. Tri An.

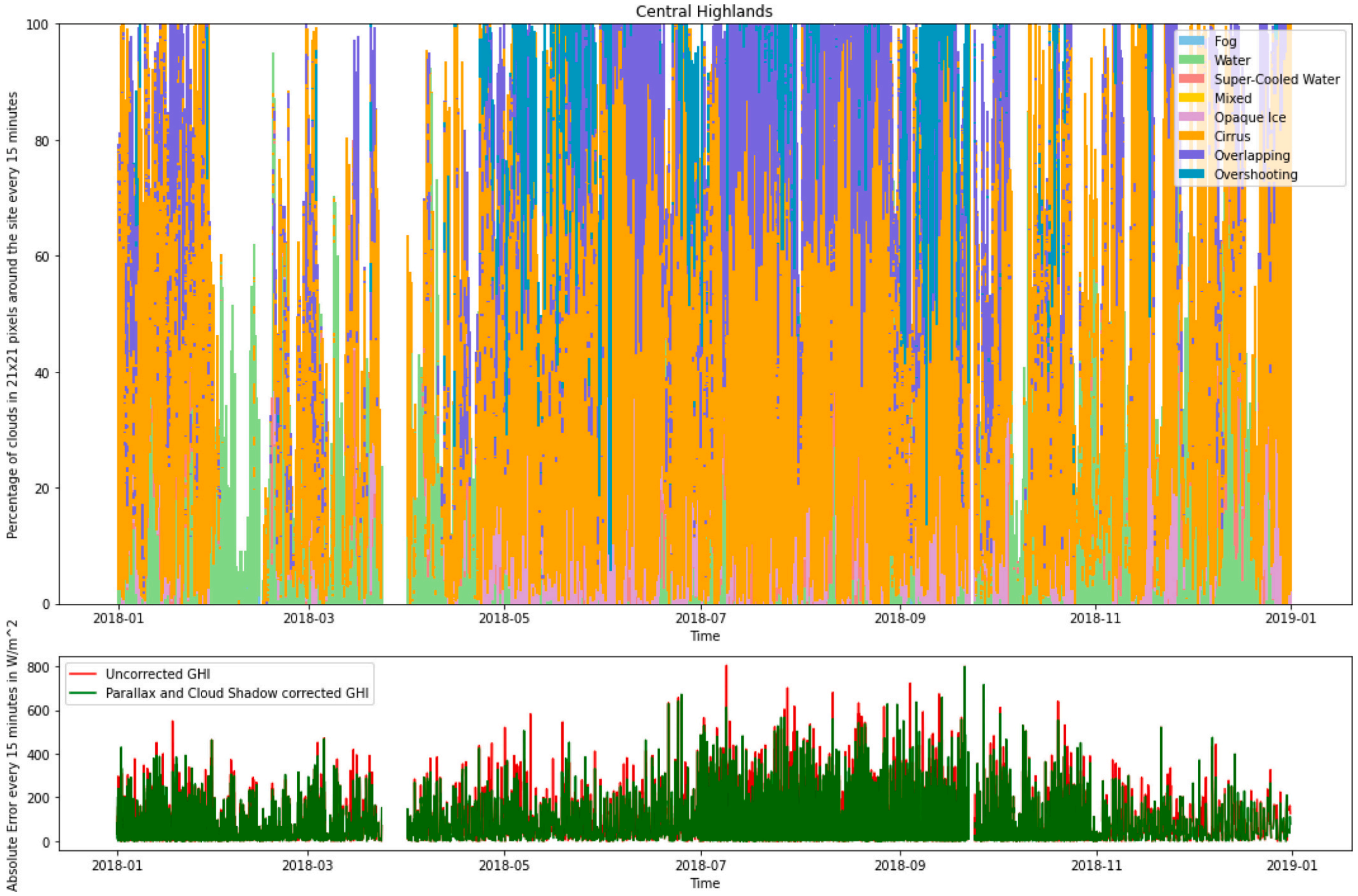

Fig. A.5. Central Highlands.

Appendix B. Variation of ramp score with τ at all the individual sites

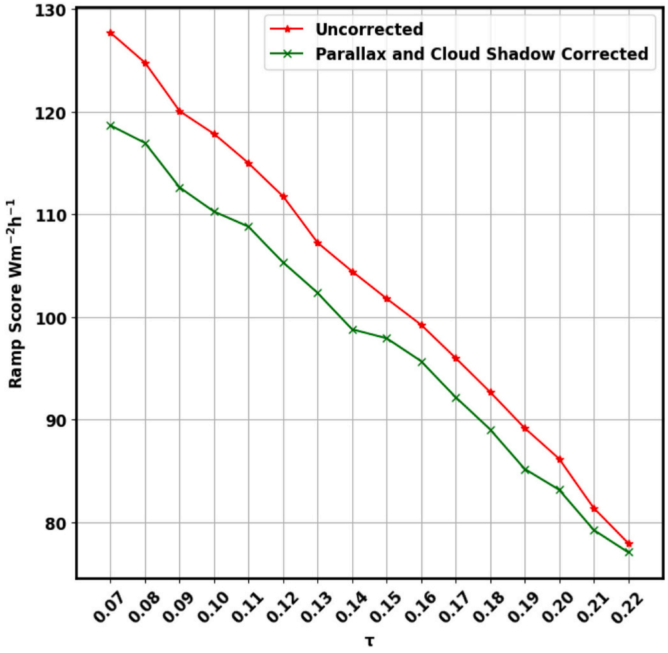

Fig. B.1. Gurgaon.

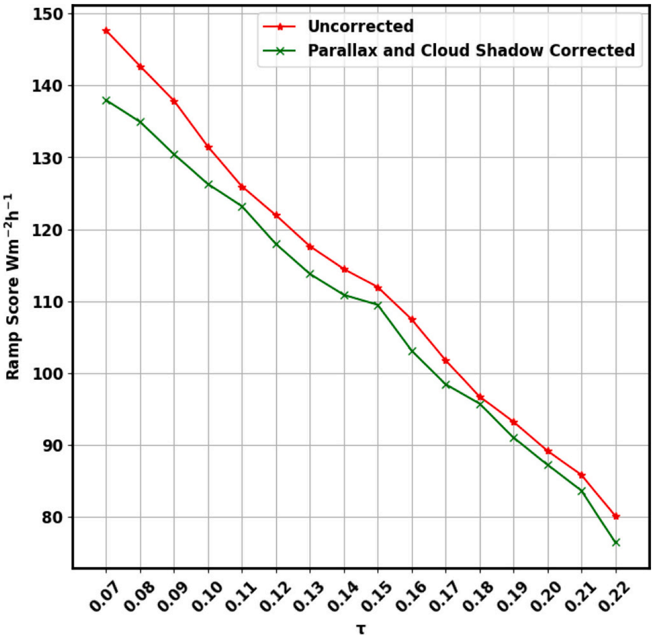

Fig. B.2. Tiruvallur.

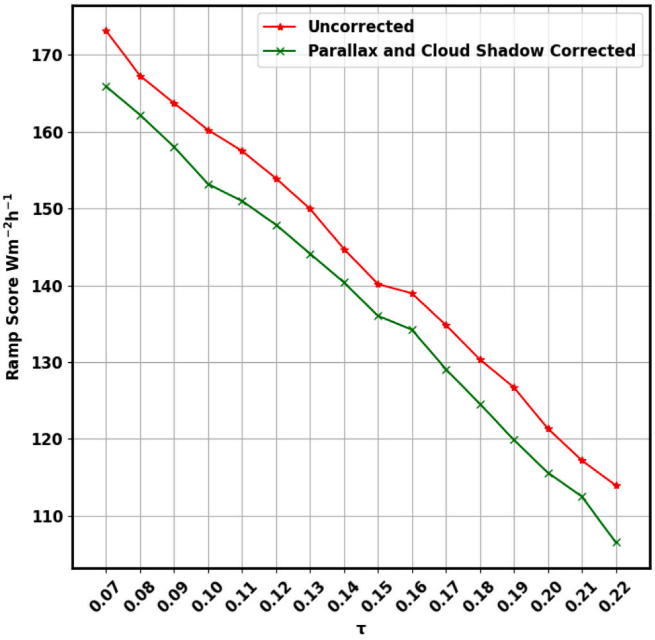

Fig. B.3. Feni.

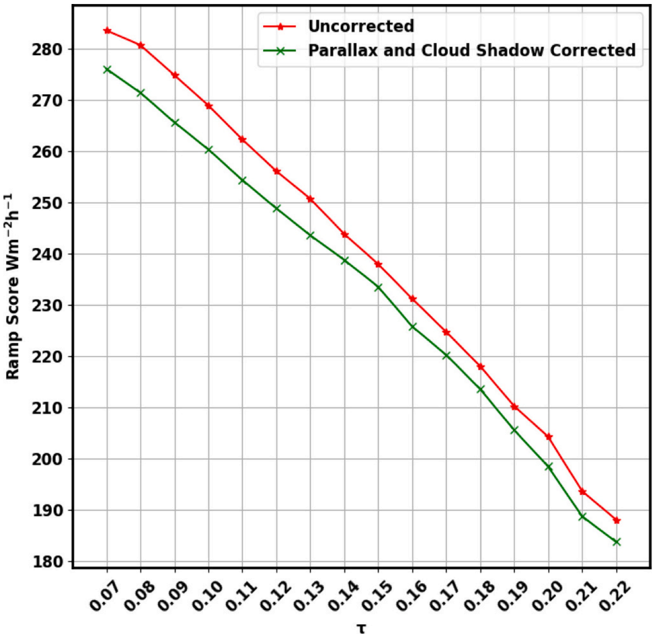

Fig. B.4. Central Highlands.

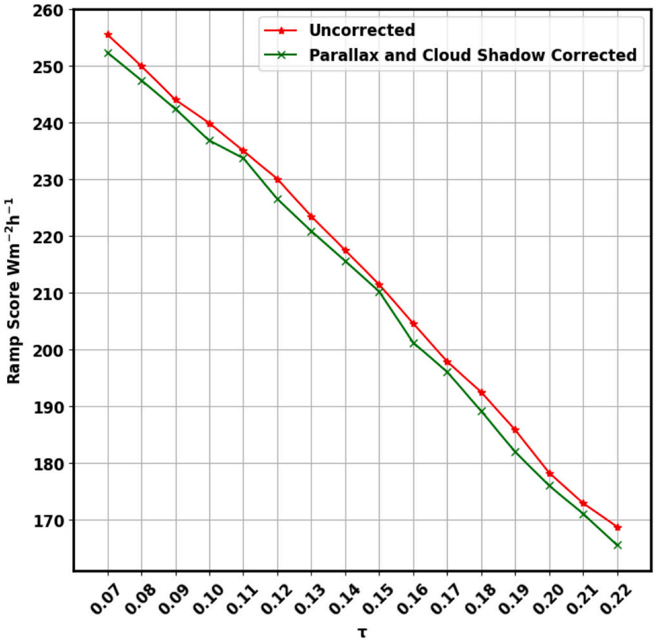

Fig. B.5. Tri An.

Appendix C. Filtering datapoints based on the uncertainty in pyranometer measurement

Based on Kratzenberg et al. [82], the maximum uncertainty in an individual pyranometer measurement is reported to be approximately 3.7 %. To assess the improvements in relative RMSE and MAE under this constraint, the dataset is filtered to include only those time points where the change in GHI after applying the correction exceeded 3.7 %, relative to the pyranometer measurement. This ensures that any observed change in the error metrics is larger than what can be theoretically attributed to measurement noise.

The relative RMSE and MAE on the filtered subset shows an even greater improvement due to the corrections across all validation sites (see Tables C.1. and C.2). For sites with similar satellite viewing zenith angles (see Table 1), the corrected Heliosat-3 estimates still outperforms both CAMS and NSRDB. In fact, the improvement relative to CAMS and NSRDB becomes even more pronounced in this filtered subset.

It can be observed that restricting the analysis to only those data points where the GHI change exceeds 3.7 % results in generally higher error values, as these cases typically correspond to cloudy conditions with complex cloud distributions, where satellite-based estimates are known to be less reliable.

Table C.1
Relative RMSE in satellite estimated GHI at 15 min resolution.**

Site	Heliosat-3 Meteosat-8	Heliosat-3 Meteosat-8 with Parallax and Shadow Correction	NSRDB Meteosat-8	NSRDB Himawari-8	CAMS Himawari-8
Gurgaon	47.1% / 17.1%	40.0% / 15.5%	51.5% / 19.8%	Not Available	Not Available
Tiruvallur	31.6% / 13.8%	26.7% / 12.8%	34.9% / 16.9%	Not Available	Not Available
Feni	45.1% / 26.3%	40.5% / 24.4%	50.8% / 31.4%	54.7% / 34.6%	43.4% / 26.9%
Central Highlands	42.7% / 32.4%	38.9% / 30.1%	Not Available	37.6% / 29.0%	33.9% / 26.1%
Tri An	41.3% / 31.3%	37.8% / 29.3%	Not Available	36.3% / 27.7%	32.2% / 24.8%

Table C.2
Relative MAE in satellite estimated GHI at 15 min resolution.**

Site	Heliosat-3 Meteosat-8	Heliosat-3 Meteosat-8 with Parallax and Shadow Correction	NSRDB Meteosat-8	NSRDB Himawari-8	CAMS Himawari-8
Gurgaon	32.7% / 8.2%	27.1% / 7.6%	35.4% / 10%	Not Available	Not Available
Tiruvallur	21.8% / 6.4%	18.5% / 6%	24.8% / 8.2%	Not Available	Not Available
Feni	30.4% / 16.6%	27.4% / 15.7%	35% / 20.2%	38.4% / 23.2%	29.5% / 16.5%
Central Highlands	29.9% / 21.5%	27.6% / 20.4%	Not Available	27% / 19.5%	23.3% / 16.8%
Tri An	28.8% / 21.4%	26.3% / 20.1%	Not Available	25.8% / 18.8%	21.5% / 15.5%

** Considering all daytime datapoints that passed the quality check.
** Considering only those datapoints where the GHI change after applying the corrections is more than 3.7%, with respect to the pyranometer measurement

Appendix D. Sensitivity of the corrections to noise in the input cloud top height data

Due to the unavailability of a spatially dense Ceilometer network in South and Southeast Asia capable of providing ground-truth cloud top height (CTH) data at the pixel level across the entire satellite image section, it is infeasible to directly add noise to measured CTH values and assess the resulting impact on GHI estimation.

Therefore, Gaussian noise – varying in mean (μ) and standard deviation (σ) from 2 km to 8 km – is introduced into the satellite-estimated CTH data used as an input to the parallax correction and cloud shadow projection algorithms, and its effect on GHI estimation error is analyzed. In all cases, the final noisy CTH values are clipped so that they lie within the range of 0 to 16 km, consistent with the original dataset.

As shown in Table D.1, when Gaussian noise with a mean and standard deviation of 2 km or 4 km is added to the CTH data, the correction procedure still improves GHI estimation compared to the uncorrected Heliosat-3 values. When the noise magnitude reaches 8 km, the corrected estimates begin to show reduced accuracy relative to the uncorrected case at two of the five sites. These results demonstrate that the correction method remains robust under moderate levels of normally distributed uncertainty in CTH.

Table D.1
Variation in GHI estimation error by adding Gaussian noise to the cloud top height (CTH) data.**

Site	Heliosat-3	Heliosat-3 + Corrections	+ Gaussian Noise ($\mu = 2$ km, $\sigma = 2$ km)*	+ Gaussian Noise ($\mu = 4$ km, $\sigma = 4$ km)*	+ Gaussian Noise ($\mu = 8$ km, $\sigma = 8$ km)*
Gurgaon	17.1 %	15.5 %	15.7 %	16.0 %	16.4 %
Tiruvallur	13.8 %	12.8 %	13.1 %	13.4 %	13.8 %
Feni	26.3 %	24.4 %	25.0 %	25.7 %	26.8 %
Central Highlands	32.3 %	30.1 %	30.2 %	30.8 %	31.5 %
Tri An	31.3 %	29.3 %	30.1 %	30.7 %	31.0 %

** "+ Noise ($\mu = x$ km, $\sigma = x$ km)" refers to adding Gaussian noise with $\mu = \sigma = x$ km to the satellite-estimated CTH data. All resulting CTH values were clipped to lie within 0–16 km.

Data availability

Data will be made available on request.

References

[1] UN. Transforming our World: The 2030 Agenda for Sustainable Development. https://sdgs.un.org/publications/transforming-our-world-2030-agenda-sustainable-development-17981; 2015.

[2] IEA. Renewables 2021. Paris: International Energy Agency; 2021. https://www.iea.org/reports/renewables-2021.

[3] Julien SA, Sajadi A, Hodge BM. Hierarchical control of utility-scale solar pv plants for mitigation of generation variability and ancillary service provision. IEEE Trans Sustain Energy 2022;13(3):1383–95.

[4] Nespoli A, Niccolai A, Ogliari E, Perego G, Collino E, Ronzio D. Machine learning techniques for solar irradiation nowcasting: cloud type classification forecast through satellite data and imagery. Appl Energy 2022;305:117834.

[5] Wang F, Li J, Zhen Z, Wang C, Ren H, Ma H, et al. Cloud feature extraction and fluctuation pattern recognition based ultrashort-term regional PV power forecasting. IEEE Trans Ind Appl 2022;58(5):6752–67. https://doi.org/10.1109/TIA.2022.3186662.

[6] Mitra I, Heinemann D, Ramanan A, Kaur M, Sharma SK, Tripathy SK, et al. Short-term PV power forecasting in India: recent developments and policy analysis. Int J Energy Environ Eng 2022;13(2):515–40.

[7] Kamath HG, Srinivasan J. Validation of global irradiance derived from INSAT-3D over India. Sol Energy 2020;202(15):45–54.

[8] Vignola FE, McMahan AC, Grover CN. Bankable Solar-Radiation Datasets. In: Kleissl J, editor. Solar Energy Forecasting and Resource Assessment. Elsevier, Ch. 5; 2013. p. 97–131.

[9] Ohtake H, Uno F, Oozeki T, Yamada Y, Takenaka H, Nakajima TY. Estimation of satellite-derived regional photovoltaic power generation using a satellite-estimated solar radiation data. Energy Sci Eng 2018;5:570–83.

[10] Jamaly M, Bosch JL, Kleissl J. Aggregate ramp rates of distributed photovoltaic systems in San Diego County. IEEE Trans Sustain Energy 2013;4(2):519–26.

[11] Gautier C, Diak G, Masse S. A simple physical model to estimate incident solar radiation at the surface from GOES satellite data. J Appl Meteorol Climatol 1980;19(8):1005–12.

[12] Nga PTT, Hao NTP, Cong NT, Hang VT, Ha PT, Nakamura K. Evaluation of solar radiation estimated from himawari-8 satellite over Viet Nam region *Vietnam*. J Sci Technol 2019;58(3A):20–32.

[13] Ohtake H, Uno F, Oozeki T, Yamada Y, Takenaka H, Nakajima TY. A case study of photovoltaic power generation and its future ramp possibility for Tokyo electric power area. IFAC-PapersOnLine 2018;51(28):645–50.

[14] Vallance L, Charbonnier B, Paul N, Dubost S, Blanc P. Towards a standardized procedure to assess solar forecast accuracy: a new ramp and time alignment metric. Sol Energy 2017;150:408–22.

[15] Roy A, Hammer A, Heinemann D, Lünsdorf O, Lezaca J. Impact of tropical convective conditions on solar irradiance forecasting based on cloud motion vectors. Environ Res Lett 2022;17(10):104048.

[16] Tegtmeier S, Anstey J, Davis S, Dragani R, Harada Y, Ivanciu I, et al. Temperature and tropopause characteristics from reanalyses data in the tropical tropopause layer. Atmos Chem Phys 2020;20(2):753–70.

[17] Evan S, Brioude J, Rosenlof K, Davis SM, Vömel H, Héron D, et al. Effect of deep convection on the tropical tropopause layer composition over the Southwest Indian Ocean during austral summer. Atmos Chem Phys 2020;20(17):10565–86.

[18] Hoffmann L, Spang R. An assessment of tropopause characteristics of the ERA5 and ERA-interim meteorological reanalyses. Atmos Chem Phys 2022;22(6):4019–46.

[19] Forstinger A, Wilbert S, Jensen AR, Kraas B, Fernández-Peruchena C, Gueymard C, Ronzio D, Yang D, Collino E, Polo Martinez J, Ruiz-Arias JA. Worldwide benchmark of modelled solar irradiance data annex. Worldwide benchmark of modelled solar irradiance data. annex 2023.

[20] Devasthale A, Grassl H. A daytime climatological distribution of high opaque ice cloud classes over the Indian summer monsoon region observed from 25-year AVHRR data. Atmos Chem Phys 2009;9(12):4185–96.

[21] Fan J, Leung LR, Rosenfeld D, Chen Q, Li Z, Zhang J, et al. Microphysical effects determine macrophysical response for aerosol impacts on deep convective clouds. Proc Natl Acad Sci USA 2013;110(48):E4581–90.

[22] Chantraket P, Intaracharoen P, Kirtsaeng S. Analysis of Rainstorm Characteristics in Eastern Regions of Thailand. Int J Appl Sci Innov 2016;1:58–70.

[23] Farukh M A, Islam M A and Uddin M N Synoptic climatology of pre-monsoon frequent lightning events in Bangladesh Nat Hazards 116 1053–1070.

[24] Saha TR, Quadir DA. Variability and trends of annual and seasonal thunderstorm frequency over Bangladesh. Int J Climatol 2016;36(14):4651–66.

[25] Cebecauer T, Šúri M, Gueymard CA. Uncertainty sources in satellite-derived direct normal irradiance: How can prediction accuracy be improved globally. In: Proceedings of the SolarPACES Conference, Granada, Spain. Vol. 2023; 2011.

[26] Demain C, Journée M, Betrand C. Sensitivity of the RMI'S MAGIC/ Heliosat-2 method to relevant input data. Adv Sci Res 2013;10:7–13.

[27] Harsarapama AP, Aryani DR, Rachmansyah D. Open-source satellite-derived solar resource databases comparison and validation for Indonesia. J Renew Energy 2020:1–14.

[28] Journée M, Stöckli R, Bertrand C. Sensitivity to spatio-temporal resolution of satellite-derived daily surface solar irradiation. Remote Sens Lett 2012;3(4):315–24.

[29] Loghmari I, Timoumi Y. Improvement global solar radiation estimation. IET Renew Power Gener 2017;11(7):996–1004.

[30] Perez R, Kivalov S, Schlemmer J, Hemker Jr K, Renné D, Hoff TE. Validation of short and medium term operational solar radiation forecasts in the US. Sol Energy 2010;84(12):2161–72.

[31] Qu Z, Gschwind B, Lefevre M, Wald L. Improving HelioClim-3 estimates of surface solar irradiance using the McClear clear-sky model and recent advances in atmosphere composition. Atmos Meas Tech 2014;7:3927–33.

[32] Qu Z, Oumbe A, Blanc P, Espinar B, Gesell G, Gschwind B, et al. Fast radiative transfer parameterization for assessing the surface solar irradiance: the Heliosat-4 method. Meteorol Z/Contr Atm Sci 2016;26(1):33–57.

[33] Sengupta M, Xie Y, Lopez A, Habte A, Maclaurin G, Shelby J. The National Solar Radiation Data Base (NSRDB). Renew Sust Energ Rev 2018;89:51–60.

[34] Yagli GM, Yang D, Gandhi O, Srinivasan D. Can we justify producing univariate machine-learning forecasts with satellite-derived solar irradiance? Appl Energy 2019;259:114122.

[35] Kim CK, Kim HG, Kang YH, Yun CY. Toward improved solar irradiance forecasts: comparison of the global horizontal irradiances derived from the COMS satellite imagery over the Korean Peninsula. Pure Appl Geophys 2017;174(7):2773–92.

[36] Sankhala DK, Deb SK, Sharma SK, Lal S. Inter-comparison of INSAT-3D atmospheric motion vectors with cloud-base height from a ceilometer. Int J Remote Sens 2020;41(8):2946–61.

[37] Nouri B, Kuhn P, Wilbert S, Hanrieder N, Prahl C, Zarzalejo L, et al. Cloud height and tracking accuracy of three all sky imager systems for individual clouds. Sol Energy 2019;177:213–28.

[38] Dybbroe A, Karlsson KG, Thoss A. NWCSAF AVHRR cloud detection and analysis using dynamic thresholds and radiative transfer modeling. Part I: Algorithm description. J Appl Meteorol Climatol 2005;44(1):39–54.

[39] Randriamamplanina R, Nagy J, Balogh T, Kerényi J. Determination of cloud top height using meteorological satellite and radar data. Phys Chem Earth Part B: Hydrol, Oceans Atmos 2000;25(10−12):1103–6.

[40] Schmetz J, Holmlund K. Operational cloud motion winds from Meteosat and the use of cirrus clouds as tracers. Adv Space Res 1992;12(7):95–104.

[41] Lonitz K, Horváth Á. Comparison of MISR and Meteosat-9 cloud-motion vectors. J Geophys Res Atmos 2011;116(D24).

[42] Dürr B, Zelenka A, Müller R, Philipona R. Verification of CM-SAF and MeteoSwiss satellite based retrievals of surface shortwave irradiance over the alpine region. Int J Remote Sens 2010;31(15):4179–98.

[43] Marie-Joseph I, Linguet L, Marie-Line G, Wald L. On the applicability of the Heliosat-2 method to assess the surface solar irradiance in the intertropical convergence zone, French Guiana. Int J Remote Sens 2013;34(8):3012–27.

[44] Wu E, Clemesha RES, Kleissl J. Coastal stratocumulus cloud edge forecasts. Sol Energy 2018;164:355–69.

[45] Sossan F. Solar irradiance estimations for modelling the variability of photovoltaic generation and assessing violations of grid constraints: a comparison between satellite and pyranometers measurements with load flow simulations. J Renew Sustain Energy 2019;11(5):056103.

[46] Kallio-Myers V, Riihelä A, Lahtinen P, Lindfors A. Global horizontal irradiance forecast for Finland based on geostationary weather satellite data. Sol Energy 2020;198:68–80.

[47] Tatsiankou V, Hinzer K, Beal R, Schriemer H. High latitude and ground assessment of NSRDB V3 irradiance using sky condition data. In: 2021 IEEE 48th photovoltaic specialists conference (PVSC); 2021. p. 0726–8.

[48] Deneke HM, Feijt AJ, Roebeling RA. Estimating surface solar irradiance from Meteosat SEVIRI-derived cloud properties. Remote Sens Environ 2008;112: 3131–41.

[49] Deneke HM, Knap WH, Simmer C. Multiresolution analysis of the temporal variance and correlation of transmittance and reflectance of an atmospheric column. J Geophys Res 2009;114:D17206. https://doi.org/10.1029/2008JD011680.

[50] Lorenzo AT, Morzfeld M, Holmgren WF, Cronin AD. Optimal interpolation of satellite and ground data for irradiance nowcasting at city scales. Sol Energy 2017; 144:466–74.

[51] Deneke H, Barrientos-Velasco C, Bley S, Hünerbein A, Lenk S, Macke A, et al. Increasing the spatial resolution of cloud property retrievals from Meteosat SEVIRI by use of its high-resolution visible channel: implementation and examples. Atmos Meas Tech 2021;14:5107–26. https://doi.org/10.5194/amt-14-5107-2021.

[52] Li S, Sun D, Yu Y. Automatic cloud-shadow removal from flood/ standing water maps using MSG/ SEVIRI imagery. Int J Remote Sens 2013;34(15):5487–502.

[53] Bieliński T. A Parallax shift effect correction based on cloud height for geostationary satellites and radar observations. Remote Sens 2020;12(3):365.

[54] Vicente GA, Davenport JC, Scofield RA. The role of orographic and parallax corrections on real-time high-resolution satellite rainfall rate distribution. Int J Remote Sens 2002;23(2):221–30.

[55] Beyer HG, Costanzo C, Heinemann D. Modifications of the Heliosat procedure for irradiance estimates from satellite images. Sol Energy 1996;56(3):207–12.

[56] Miller SD, Rogers MA, Haynes JM, Sengupta M, Heidinger AK. Short-term solar irradiance forecasting via satellite/model coupling. Sol Energy 2018;168:102–17.

[57] Bright JM. Solcast: validation of a satellite-derived solar irradiance dataset. Sol Energy 2019;189:435–49.

[58] Gschwind B, Wald L, Blanc P, Lefèvre M, Schroedter-Homscheidt M, Arola A. Improving the McClear model estimating the downwelling solar radiation at ground level in cloud-free conditions–McClear-v3. Meteorol Z 2019;28(2).

[59] EUMETSAT. Conversion from radiances to reflectances for SEVIRI warm channels EUMETSAT Doc. EUM/MET/TEN/12/0332. 2012.

[60] Hammer A, Kühnert J, Weinreich K, Lorenz E. Short-term forecasting of surface solar irradiance based on Meteosat-SEVIRI data using a nighttime cloud index. Remote Sens 2015;7(7):9070–90.

[61] Dumortier D. Modelling global and diffuse horizontal irradiances under cloudless skies with different turbidities. In: Final report JOU2-CT92–0144, daylight II. Vaulx-enVelin, France: Technical Report Ecole Nationale des Travaux Publics de l'État; 1995.

[62] Remund J, Wald L, Lefèvre M, Ranchin T, Page JH. Worldwide Linke turbidity information. In: ISES solar world congress; 2003. p. 400.

[63] Driemel A, Augustine J, Behrens K, Colle S, Cox C, Cuevas-Agulló E, et al. Baseline surface radiation network (BSRN): structure and data description (1992–2017). Earth Syst Sci Data 2018;10(3):1491–501.

[64] Kumar A, Gomathinayagam S, Giridhar G, Mitra I, Vashistha R, Meyer R, et al. Field experiences with the operation of solar radiation resource assessment stations in India. Energy Procedia 2014;49:2351–61.

[65] Forstinger A, Wilbert S, Jensen AR, Kraas B, Peruchena CF, Gueymard CA, et al. Expert quality control of solar radiation ground data sets. In: international solar energy society ISES solar world congress 2021; 2021. p. 1037–48.

[66] Loo YY, Billa L, Singh A. Effect of climate change on seasonal monsoon in Asia and its impact on the variability of monsoon rainfall in Southeast Asia. Geosci Front 2015;6(6):817–23.

[67] Stowe LL, Davis PA, McClain EP. Scientific basis and initial evaluation of the CLAVR-1 global clear/cloud classification algorithm for the Advanced Very High Resolution Radiometer. Journal of atmospheric and oceanic technology 1999 Jun; 16(6):656–81.

[68] Vemury S, Stowe LL, Anne VR. AVHRR pixel level clear-sky classification using dynamic thresholds (CLAVR-3). J Atmos Ocean Technol 2001;18(2):169–86.

[69] Azam F, Betcke J, Schroedter-Homscheidt M, Lefèvre M, Saint-Drenan YM, Saboret L, Andrietti S. CAMS Solar Radiation Service, variability-based evaluation and service evolution to other parts of globe. InESA Living Planet Symposium 2022:2022.

[70] Borde R, Dubuisson P. Cloud top height estimation using simulated METEOSAT-8 radiances. Procs SPIE 2007;6745.

[71] EUMETSAT. Cloud top height: product guide EUMETSAT Doc. EUM/TSS/MAN/14/786420. 2017.

[72] EUMETSAT. MSG meteorological products extraction facility algorithm specification document EUMETSAT Doc. EUM/MSG/SPE/022. 2015.

[73] EUMETSAT. TD 16: Meteosat data collection and distribution service Doc. EUM/OPS/DOC/08/0325. 2011.

[74] Wolf R, Just D. LRIT/HRIT global specification *Coordination Group for Meteorological Satellites* EUMETSAT CGMS 03 Technical Report 2.6. 1999.

[75] McConnell TR. Harvesting Lunar Eccentricity?. http://72.167.220.210/eccentric.pdf; 2014.

[76] Blanc P, Wald L. The SG2 algorithm for a fast and accurate computation of the position of the Sun for multi-decadal time period. Sol Energy 2012;86(10): 3072–83.

[77] Bristol EH. Swinging door trending: adaptive trend recording? ISA Natl Conf Proc 1990;45:749–53.

[78] Pfeifroth U, Kothe S, Drücke J, Trentmann J, Schröder M, Selbach N, et al. Surface radiation data set – Heliosat (SARAH) – Edition 3. In: Satellite Application Facility On Climate Monitoring; 2023.

[79] Wang M, Su J, Xu Y, Han X, Peng N, Ge J. Radiative contributions of different cloud types to regional energy budget over the SACOL site. Clim Dyn 2023;61(3): 1697–715.

[80] Ri A, Ma R, Shang H, Xu J, Tana G, Shi C, He J, Bao Y, Chen L and Letu H Influence of multilayer cloud characteristics on cloud retrieval and estimation of surface downward shortwave radiation Front Environ Sci **10** 857414.

[81] Teng S, Liu C, Tan Z, Li J, Xu N, Hu X, et al. A multispectral method for retrieving overlapping cloud top heights from passive radiometers. Remote Sens Environ 2023;286(1):113425.

[82] Kratzenberg MG, Beyer HG, Colle S, Albertazzi A. Uncertainty calculations in pyranometer measurements and application. In: Proceedings of the ASME 2006 international solar energy conference. American Society of Mechanical Engineers; 2006. p. 689–98.